Assessing impacts of canopy 3D structure on chlorophyll fluorescence radiance and radiative budget of deciduous forest stands using DART

Omar Regaieg, Tiangang Yin, Zbyněk Malenovský, Bruce Cook, Douglas Morton, Jean-Philippe Gastellu-Etchegorry

Remote Sensing of Environment 265 (2021) 112673

Contents lists available at ScienceDirect

Remote Sensing of Environment

journal homepage: www.elsevier.com/locate/rse

Assessing impacts of canopy 3D structure on chlorophyll fluorescence radiance and radiative budget of deciduous forest stands using DART

Omar Regaieg [a,*], Tiangang Yin [b,c,**], Zbyněk Malenovský [d], Bruce D. Cook [b], Douglas C. Morton [b], Jean-Philippe Gastellu-Etchegorry [a]

[a] Centre d'Etudes Spatiales de la Biosphere – UT3, CNES, CNRS, IRD, Université de Toulouse, 31401 Toulouse Cedex 9, France
[b] NASA Goddard Space Flight Center, Biospheric Sciences Laboratory, 8800 Greenbelt Rd, Greenbelt, MD 20771, USA
[c] Earth System Science Interdisciplinary Center, University of Maryland, College Park, MD 20740-3823, USA
[d] School of Geography, Planning, and Spatial Sciences, University of Tasmania, Private Bag 76, Hobart, TAS 7001, Australia

ARTICLE INFO

Editor: Jing M. Chen

Keywords:
SIF
Radiative transfer modeling
Radiative budget
Photosynthetic active radiation
Escape factor
3D forest architecture
Wood

ABSTRACT

Although remote sensing (RS) of solar-induced chlorophyll fluorescence (SIF) is increasingly used as a valuable source of information about vegetation photosynthetic activity, the RS SIF observations are significantly influenced by canopy-specific structural features (*i.e.*, canopy architecture including leaf area index and presence of woody components), atmospheric conditions during their acquisition (*e.g.*, proportion of direct and diffuse irradiance) and observational geometric configurations (*e.g.*, sun and viewing directions). Radiative transfer (RT) models have the potential to provide a better understanding of the canopy structural effects on the SIF emission and RS signals. Here, we used the DART model to assess the daily influence, from morning to evening, of forest 3D architecture on SIF nadir radiance, emission, escape factor and nadir yield of eight 100 m × 100 m forest study plots established in a temperate deciduous forest of the Smithsonian Environmental Research Center (Edgewater, MD, USA). The 3D architecture of each plot was derived from airborne LiDAR. DART simulations of these 3D forest plots and their 1D (*i.e.*, vertical profile of sun-adapted and shade-adapted leaves) and 0D (*i.e.*, homogeneous layer of sun-adapted leaves above an homogeneous layer of shade-adapted leaves) abstractions were compared to assess the relative errors (ε_{1D_3D} and ε_{0D_3D}) associated with horizontal and vertical structural heterogeneity, respectively. Forest 3D structure, especially horizontal heterogeneity, had a great influence on forest nadir SIF radiance, resulting in ε_{1D-3D} up to 55% at 8:00 and 18:00 (*i.e.*, for oblique sun directions). The key indicators of this impact, in the descending order of importance, were the SIF escape factor (ε_{1D-3D} up to 40%), the attenuation of incident photosynthetically active radiation (ε_{1D-3D} less than 5%), and the SIF emission yield (ε_{0D-3D} less than 2%). The influence of forest architecture on the nadir SIF escape factor and SIF yield (ε_{1D_3D} up to 40%) varied over time, with differences in forest stand structure, and per spectral domain, being always larger between 640 and 700 nm than between 700 and 850 nm. In addition, woody elements demonstrated a large influence on forest SIF radiance due to their "shading" effect (ε up to 17%) and their "blocking" effect (ε ≈ 10%), both of them higher for far-red than for red SIF. These results underline the importance of 3D forest canopy architecture, especially 2D heterogeneity, and inclusion of woody elements in RT modeling used for interpretation of the RS SIF signal, and subsequently for the estimation of gross primary production and detection of vegetation stress.

* Corresponding author.
** Corresponding author at: NASA Goddard Space Flight Center, Biospheric Sciences Laboratory, 8800 Greenbelt Rd, Greenbelt, MD 20771, USA.
E-mail addresses: omar.regaieg@gmail.com (O. Regaieg), tiangang.yin.85@gmail.com (T. Yin).

https://doi.org/10.1016/j.rse.2021.112673
Received 20 May 2021; Received in revised form 8 August 2021; Accepted 20 August 2021
Available online 28 August 2021

1. Introduction

Solar-induced chlorophyll fluorescence (SIF) is a photoprotective electromagnetic radiation emitted by chlorophyll molecules in response to absorption of photosynthetically active radiation (PAR) by green vegetation. Since the energy emitted as SIF is complementary to the energy entering the photochemical processes and the excessive energy dissipated as heat (Baker, 2008; Mohammed et al., 2019), it is considered as an indicator of the functional state of plant photosynthesis (Baker, 2008). SIF measurements are complicated by the fact that SIF represents only a small fraction of absorbed PAR and spectrally overlaps with radiation reflected by Earth surface elements and the atmosphere. However, the improvement of remote sensing (RS) optical sensors and techniques for retrieving the SIF signal (Meroni et al., 2009; Mohammed et al., 2019) has opened new avenues for monitoring the functional state of vegetation. SIF can be used to track actual photosynthetic efficiency (Rossini et al., 2015; Campbell et al., 2019; Yang et al., 2021), to improve assessment of plant gross primary production (Guanter et al., 2014; Z. Liu et al., 2019), and to detect vegetation stress (Ač et al., 2015). This diverse potential of SIF for vegetation monitoring spurred the development of methods for space-borne measurements and new satellite missions, such as the FLuorescence EXplorer (FLEX) selected by the European Space Agency (ESA) as its 8th Earth explorer scientific mission (Drusch et al., 2017).

Besides plant photosynthetic activity, SIF observations are impacted by other confounding factors, notably the structure of vegetation canopies (Fournier et al., 2012; Migliavacca et al., 2017) and PAR availability. They are of SIF also influenced by sun-canopy-sensor angular and directional effects (Zhang, Zhang, Porcar-Castell, et al., 2020; Zhang, Zhang, Zhang, et al., 2020), and are driven by wavelength-dependent phenomena of SIF emission, scattering, and re-absorption. For instance, Fournier et al. (2012) found that the red-to-far-red fluorescence ratio could decrease by a factor of two between the leaf level and the canopy level, due to a higher absorption of red SIF by the vegetation canopy. Therefore, accurate interpretation and use of SIF RS observations require understanding of three consecutive processes: i) interception of photosynthetically active radiation (PAR; 400 - 750 nm) and its absorption by foliar elements ($APAR_{green}$; $W.m^{-2}$), due to chlorophyll pigments in leaves, ii) leaf SIF emission from photosystems I and II (PSI and PSII) in thylakoid membranes, due to $APAR_{green}$, and iii) propagation of the SIF radiation through the canopy, including its scattering and absorption by different canopy elements, *i.e.*, leaves, woody elements, litter, bare soil, and others (van der Tol et al., 2019).

Radiative transfer models (RTMs) are powerful tools used for various vegetation RS applications, ranging from sensitivity analyses (Malenovský et al., 2008) to quantitative retrievals of models' biophysical inputs (Brede et al., 2020; Verrelst et al., 2019). The increasing need for understanding and interpreting the SIF signal at canopy level resulted in coupling canopy RTMs with a leaf-level SIF model, most frequently with Fluspect (Vilfan et al., 2016). The pioneer in one-dimensional (1D) SIF canopy modeling is SCOPE (van der Tol et al., 2009). Based on SAIL RTM (Verhoef, 1984) and coupled with leaf-level SIF and biochemistry models, SCOPE models photosynthesis and the full energy balance (Damm et al., 2015; Migliavacca et al., 2017; Verrelst et al., 2015, 2016). Despite its extension to vertically heterogeneous canopies (Yang et al., 2017), SCOPE's 1D formulation makes it less suitable for structurally complex and spatially heterogeneous canopies, such as forests. This explains the recent development of three-dimensional (3D) SIF RTMs, such as FluorFLIGHT (Hernández-Clemente et al., 2017), based on the 3D FLIGHT model (North, 1996), FLiES-SIF (Sakai et al., 2020) based on the FLiES model (Kobayashi & Iwabuchi, 2008) that simulate SIF for tree canopies, FluorWPS (Zhao et al., 2016) based on the WPS model (Zhao et al., 2015) designed to simulate SIF of structurally complex canopies and the FluLCVRT model (Kallel, 2020) that simulates SIF for 3D canopies including 3D leaf-level SIF modeling. The work presented in this paper was carried out with the 3D discrete anisotropic radiative transfer (DART) model (Gastellu-Etchegorry et al., 2017) coupled with Fluspect-Cx (Vilfan et al., 2018). DART simulates both the 3D SIF radiative budget (*i.e.,* interception, absorption, emission and scattering) and the SIF signal remotely sensed at the bottom of atmosphere (BOA) and top of atmosphere (TOA) for forest or crop canopies. It upscales leaf-level SIF to canopy SIF, while considering the user-defined leaf biochemistry and fluorescence quantum yield efficiencies of PSI and PSII, and accounting for the actual 3D vegetation architecture. DART has been cross compared with the SCOPE modeling of the same 1D vegetation scenarios (Malenovský et al., 2021), and used in various studies for sensitivity analyses of the SIF signal in architecturally complex forest canopies (W. Liu et al., 2019; Malenovský et al., 2021), scaling canopy-level SIF down to the level of photosystems (X. Liu et al., 2019), and studying the escape probability of far-red SIF from discontinuous forest canopies (W. Liu et al., 2020).

The main objective of this paper is to assess the impact of temperate deciduous forest architecture on the diurnal variability in the nadir SIF RS signal and within-canopy SIF emission by green leaves. SIF canopy signals were simulated with a new Monte Carlo mode of

DART, called DART-Lux, whereas the radiative budget of within canopy SIF emission was simulated using the standard flux tracking mode of DART, called DART-FT. (cf. section 2.1).

2. Material and methods

2.1. Discrete anisotropic radiative transfer (DART) modeling approaches

DART (https://dart.omp.eu) is a comprehensive physically based 3D RTM developed by the CESBIO Laboratory (Toulouse, France) since 1993 (Gastellu-Etchegorry et al., 1996, 2015). It is continuously improved both scientifically (*e.g.*, light polarization and radiative coupling between the atmosphere and Earth surfaces) and technically (*e.g.*, computational efficiency in terms of simulation time and computer memory). It simulates the radiative budget (RB) as well as TOA, BOA, and in-situ RS observations (*i.e.*, LiDAR and imaging spectroradiometer data, either pushbroom scanner, hemispherical or frame camera) of urban and natural landscapes from the visible to the thermal infrared spectral domains, for any experimental and instrumental configuration (solar illumination, viewing direction, atmosphere condition, spatial and spectral resolutions, etc.). DART is made of three radiative transfer modeling modules:

1. DART-FT (Flux Tracking) simulates passive optical RS signals and 3D RB, including SIF, using an adaptation of the N-flux discrete ordinates' method (Yin et al., 2013, 2015). Landscapes are simulated as the juxtaposition of planar triangular facets in 3D arrays of voxels that contain fluid and turbid medium (*i.e.*, vegetation volume statistically characterized by a leaf angular distribution (LAD) and a leaf area index (LAI) equivalent to a volume filled with an infinite number of infinitely small planar surfaces).

2. DART-RC (Ray Carlo) combines Monte Carlo (MC) and FT methods in order to simulate LiDAR signals (Gastellu-Etchegorry et al., 2016; Yin et al., 2016). 3D landscapes are simulated in the same way as for DART-FT module.

3. DART-Lux is a new module that broadens the application domain of DART to large landscapes through the introduction of a bidirectional MC modeling approach adapted from the physically based and unbiased rendering engine called LuxCoreRender (Georgiev et al., 2012; *LuxCoreRender – Open Source Physically Based Renderer*). It greatly improves the computational efficiency of simulations for large and complex landscapes. For example, the reduction of simulation time and computer memory can be over 100-times. Indeed, this DART mode only tracks radiation that impacts the signal forming the sensor observation.

Landscapes are simulated as the juxtaposition of facets and volumes filled with fluids and turbid medium. Volumes in DART-Lux can be defined independently from the 3D arrays of voxels, unlike DART-FT and RC. Although still under intensive testing, DART-Lux already simulates most RS products of DART-FT and DART-RC, including SIF and LiDAR. Presently, TOA signals are simulated using DART-FT based atmosphere modeling (Wang & Gastellu-Etchegorry, 2021). MC-based modeling of atmosphere thermal radiative transfer, as well as radiative budget are under development.

SIF modeling was initially introduced in DART-FT for vegetation canopies represented explicitly with facets (Gastellu-Etchegorry et al., 2017) and later for canopies simulated with 3D turbid voxels (Regaieg et al., 2020). More recently, SIF modeling was also implemented in DART-Lux, for both facet-based as well as turbid canopies (Regaieg et al., in preparation). As indicated above, compared to the standard DART-FT mode, DART-Lux is much more efficient in terms of computation time and required memory to simulate RS images, including SIF images. However, up to now it does not simulate the landscape RB. Therefore, in this work, we simulated SIF image observations at the spatial resolution of 1m in DART-Lux, whereas the forest RB was simulated in DART-FT at a lower spectral resolution to reduce computational demand.

The leaf radiative transfer model Fluspect-Cx, which was embedded in DART and tested by (Malenovský et al., 2021), simulates additionally to leaf spectral reflectance and transmittance optical properties the forward and backward fluorescence excitation-emission matrices per photosystem (PSI and PSII). Its inputs include contents of foliar pigments, water and dry matter, a structural parameter characterizing the leaf optical thickness, and leaf fluorescence quantum efficiencies *fqe* (*i.e.*, fraction of $APAR_{green}$ emitted as fluorescence) of a dark-adapted leaf, that are in DART referred to as PSI and PSII fluorescence yields. Leaf physiology and local climatology influence *fqe*. However, unlike the SCOPE model, DART does not contain a leaf biochemical model, and therefore cannot simulate the canopy climatic weights that condition leaf *fqe*. Therefore, in DART, *fqe* is an input parameter that can be specified per individual foliage facet, per group of foliage facets, per type of turbid medium, or as a single value for all leaf facets and turbid medium types. Groups of foliage facets can correspond, for instance, to sunlit and shaded leaves (*i.e.*, leaves irradiated by direct sun or not at a certain time), or to sun- and shade-adapted leaves (*i.e.*, leaves that have grown under and adapted to high or low light intensity such that biochemical contents vary), knowing that a sun-adapted leaf can be

momentarily a shaded leaf and vice versa. In this work, forest *fqe* values published in (W. Liu et al., 2019) are used. Although very likely differing from actual values of the study forest sites, these values are sufficiently representative to investigate the impact of forest architecture and different structures (*e.g.*, wood components) on canopy SIF signal and emission. We also note that although sun-adapted and shade-adapted *fqe*'s are considered, the actual light and temperature modulations are not. Consequently, a leaf emitted SIF is given by APAR and *fqe* per leaf adaptation.

2.2. Study sites

Eight deciduous forest sites in the Smithsonian Environmental Research Center (SERC, Edgewater, MD, USA) were selected as the study sites. The stands mainly consist of mixed-species deciduous forests of *Liquidambar styraciflua* and *Liriodendron tulipifera* for the overstory, *and C. tomentos*a, *Quercus alba*, and *F. grandifolia* for the understory (Kamoske et al., 2019; Parker, 1995). Descriptions of forest stands and management characteristics can be found in (Brush et al., 1980, Parker et al., 2001, McMahon et al., 2010). Four forest stand types were selected from the combinations of both canopy development categories ["intermediate" (I) or "mature" (M)] and experimental status categories ["control" (C) or "logged" (L)], and two sites of each type (indexed 1 and 2) were used for this study (Table 1). Therefore, the eight study sites (Figure 1) have different canopy architectures, as illustrated by their height maps (Figure 2) and LAI vertical profiles. The forest plots LI2, LM1, LM2, and, to a lesser extent, LI2, have a larger horizontal heterogeneity than the other plots. These plots also have pronounced heterogeneity, with foliage density being larger (*i.e.*, larger LAI voxel values in DART-FT) in the bottom canopy layers than in the top canopy layers. Table 2 shows the wood area density and the LAI for sun- and shade-adapted leaves (cf. Section III-1). We note that the concept of wood area density does not have an actual physical meaning linking with trunks and branches' surface areas. It is derived from leaf off G-LiHT ALS data, and used to compensate the interception contribution induced by woody part. The presence of a local topography explains why the total ground area (*i.e.*, area based on DEM; Table 2) is larger than the scene area (i.e., $100\,m \times 100\,m$). Leaf chlorophyll a+b and carotenoid contents (µg cm^{-2}) were derived from top of canopy leaf samples collected at SERC in July of 2017 (Campbell et al., 2018), and measured using established protocol described in (Campbell et al., 2007). Pigments were extracted in dimethyl sulfoxide, identified spectro-photometrically at 1-nm resolution

159 using a dual-beam spectrophotometer (Perkin-Elmer; Wellesley, MA, USA) and calculated
160 using absorption coefficients and equations described by (Wellburn, 1994).

161 Biochemical and optical properties of leaves, woody elements and soil properties used in DART
162 are listed in Table 3. The overall LAI of 3-D reconstruction has been validated against field
163 litter-collection measurements in 2012 for various voxel dimensions from 0.5m to 5m.

164

165 Table 1. Study sites' nomenclature and description.

	Abbreviations	Description
Experimental status categories	C (Control)	No known management
	L (Logged)	Selective harvest (~ 50% of basal area)
Canopy development categories	M (Mature)	~125 years-old at time of harvesting
	I (Intermediate)	~70 years old at time of harvesting

166

167 Table 2. Wood area density, LAI (per sun-/shade-adapted leaves) and DEM-derived area for each site.

Parameter/Study site	CI1	CI2	CM1	CM2	LI1	LI2	LM1	LM2
Wood area density ($m^2.m^{-2}$)	0.792	0.863	0.939	0.991	0.665	0.435	0.827	0.615
Sun-adapted LAI ($m^2.m^{-2}$)	2.916	3.093	3.697	3.160	1.964	0.951	1.341	1.920
Shade-adapted LAI ($m^2.m^{-2}$)	2.601	2.847	2.996	3.174	3.181	2.810	3.419	3.559
Area based on DEM (m^2)	12450.7	14475.9	16535.3	11297.9	17628.8	15395.0	17576.3	20142.0

168

169 Table 3. Biochemical and optical properties used in DART modeling of the study sites.

Parameter/Study site	CI1	CI2	CM1	CM2	LI1	LI2	LM1	LM2
Leaf chlorophyll a+b content ($\mu g.cm^{-2}$)	24.307	23.253	20.23	18.146	20.569	23.264	19.619	20.165
Leaf total carotenoid content ($\mu g.cm^{-2}$)	7.06	6.81	6.338	5.852	6.295	6.843	6.156	6.364
Leaf dry matter content ($g.cm^{-2}$)	0.012							
Leaf equivalent water thickness (cm)	0.009							
Leaf fluorescence quantum efficiency	PSI: 0.0053, PSII: shade-adapted: 0.0201, sun-adapted: 0.0154							
Wood optical property	Bark of *Populus tremuloides*							
Soil optical property	Loam-gravelly brown dark soil (Alfisol from the spectra library: http://speclib.jpl.nasa.gov/)							

170

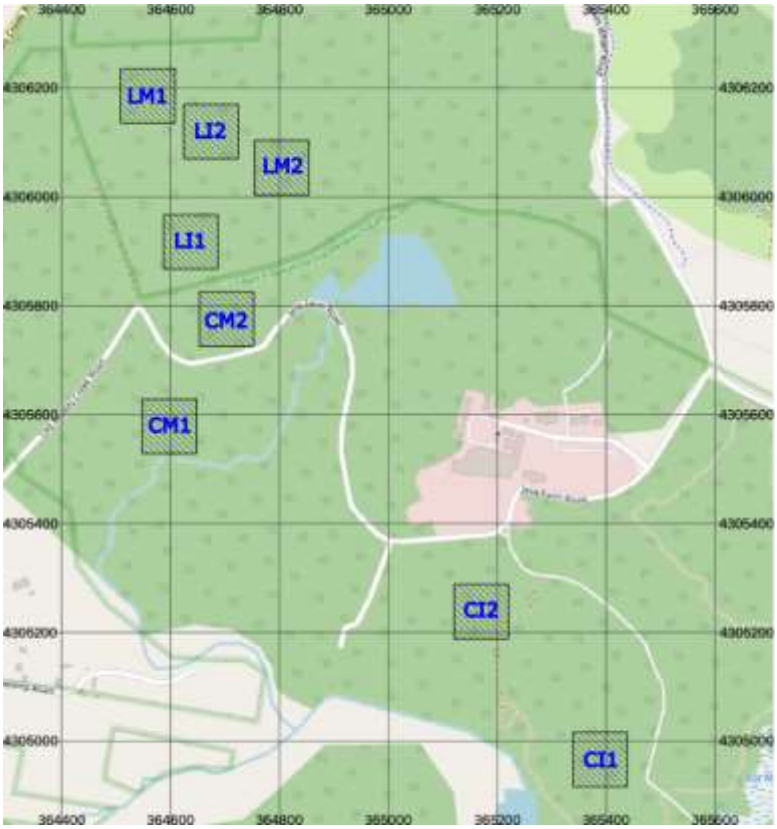

Plot Sites	Latitude	Longitude
CM1	38.8887	-76.5612
CM2	38.8904	-76.5600
CI1	38.8857	-76.5545
CI2	38.8833	-76.5520
LM1	38.8941	-76.5618
LM2	38.8930	-76.5589
LI1	38.8917	-76.5608
LI2	38.8935	-76.5604

171

172 Figure 1. Locations of SERC forest study sites (Edgewater, MD, USA) and G-Liht flight paths.

173

174 **2.3. Creation of 3D forest abstractions from airborne LiDAR acquisitions**

175 The 3D abstractions (mock-ups) of the eight forest sites were derived from 2012 multi-
176 directional and multi-temporal acquisitions by an airborne discrete-return LiDAR scanner
177 (Riegl's VQ480i), which is part of the Goddard's LiDAR, Hyperspectral and Thermal (G-LiHT)
178 Airborne Imager (Cook et al., 2013). The LiDAR acquisitions were taken during two forest
179 growth stages: i) the leaf-off stage (in March) and ii) the leaf-on stage (in June). Each
180 constructed forest mock-up ($100m \times 100m$) corresponds to a 3D array of $1m$-size voxels filled
181 with a turbid medium. The leaf angle distribution varies with height following an ellipsoidal
182 distribution generated by mean leaf incline angle from 10° at the lower canopy to 60° at the
183 upper canopy. In this experiment, we assumed an overall leaf incline angle of 57.3° over the
184 whole canopy, which may induce a slight underestimation of LAI at the upper canopy and over
185 estimation at the lower canopy in scene construction. This assumption has minor influence since
186 the change of incline angle is correlated with sun illumination, where majority of the sunlight
187 is intercepted by the leaves with larger incline angle. Since the objective was to investigate

changes in the diurnal variation of canopy SIF radiance and leaf emissions on 15 June 2017 between 7.00 and 19.00 (local time, with a time step of 1 h), the DART simulated solar zenith angles (SZA) and solar azimuth angles (SAA) were adjusted accordingly, with for example (SZA, SAA) = (76.85°, 109.51°) at 7.00, (15.62°, 5.8°) at 13.00, and (74.33°, 252.4°) at 19.00 of the local time.

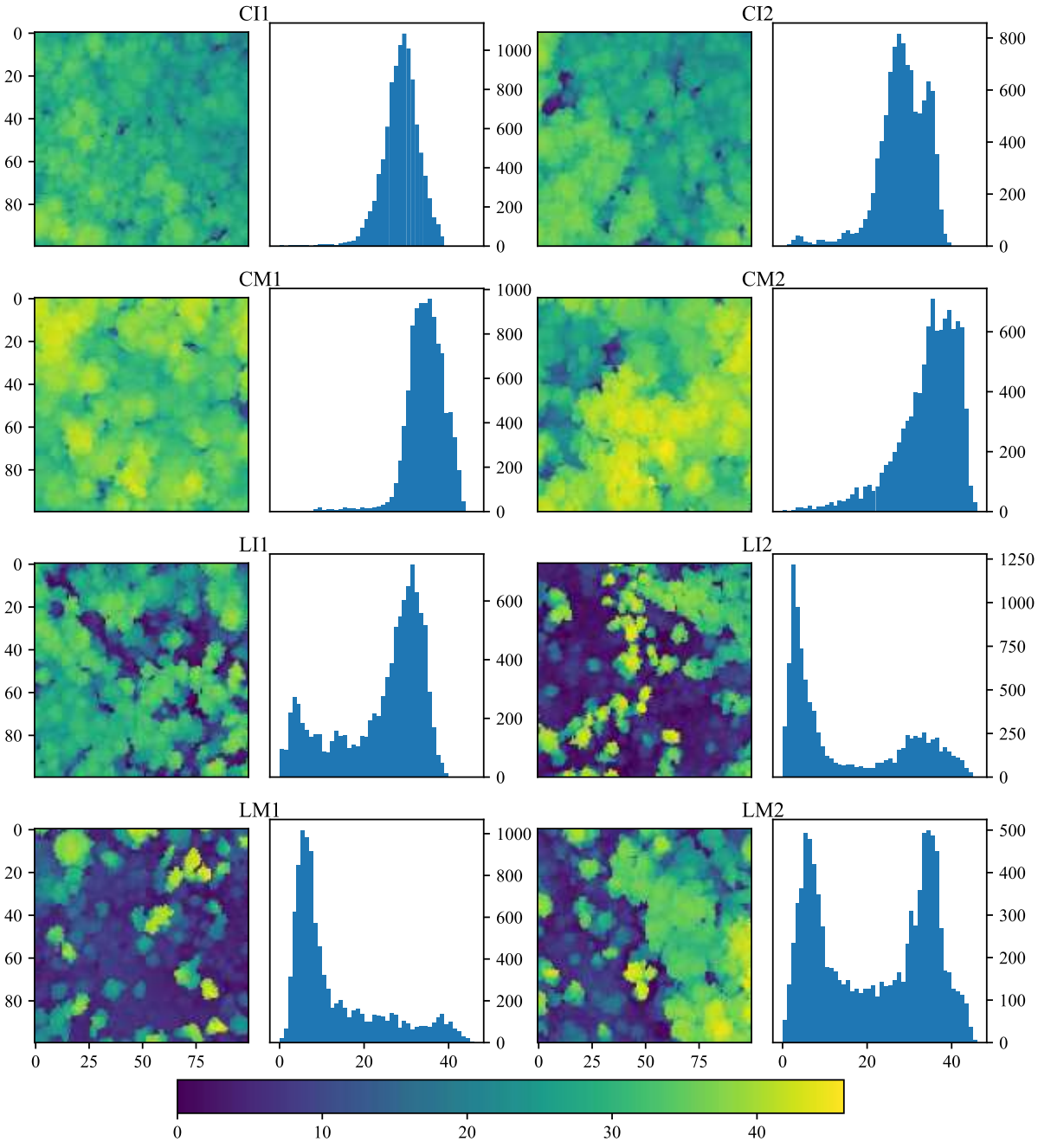

Figure 2. Maps and histograms of forest top-of-canopy height (m) for the eight forest study sites.

196 Table 4. Forest plot mean height and height standard deviation and number of pure bare ground pixels.

Plot	CI1	CI2	CM1	CM2	LI1	LI2	LM1	LM2
Mean Height (m)	28.65	28.34	34.54	34.33	23.80	15.19	13.31	21.75
Height standard deviation (m)	4.37	5.90	4.61	7.32	10.44	14.03	10.88	13.17
Number of pure bare ground pixels (out of 10 000)	2	1	2	4	89	258	8	48

197

198 **2.4. Preprocessing of modeled forest scenes**

199 Leaf biochemical and anatomical properties are adapted to the leaf exposure to sun direct and
200 scattered diffuse radiation (Givnish, 1988; Nobel, 1976). To assess 3D distribution of sun- and
201 shade-adapted foliage in each forest plot, we used DART-FT to compute hourly time series of
202 3D RB in the PAR domain from sunrise to sunset on 15 June 2012, with SZA and SAA as
203 specified in the section 2.3. The diurnal radiation intercepted by foliar elements in each turbid
204 voxel of the 3D plots computed by DART-FT was then used to classify the foliage turbid voxels
205 of each forest plot into sun- and shade-adapted foliage voxel groups. Sun- and shade-adapted leaf
206 classification methods based on thresholds on the intercepted radiation were developed for the
207 DART model for vegetation canopies simulated as facets (Malenovský et al., 2021). Here, in the
208 absence of information on the threshold definition, and for a vegetation canopy simulated as
209 turbid voxels, we chose to simply define classification decision threshold in such a way that the
210 numbers of sun-adapted voxels and shade-adapted voxels were equal. Subsequently, specific *fqe*
211 input values were assigned to the sun-adapted and shade-adapted cells (W. Liu et al., 2019)

212 Since the DART-FT mode was slow and too demanding for computer memory when simulating
213 SIF radiance of the forest plots represented by many voxels ($>10^5$) for 372 spectral bands (Table
214 5), we used the DART-Lux mode instead. As DART-Lux could at that time only simulate the
215 SIF signal of landscapes represented by geometrical facets, a "turbid-to-facet" conversion
216 procedure was designed to transform the forest turbid mock-ups (already classified into sun-
217 adapted and shade-adapted voxels) into forest 3D abstractions with leaf and woody elements
218 being represented with solid facets (cf. Appendix). DART-FT and DART-Lux give nearly
219 equivalent results in terms of canopy reflectance and SIF radiance (cf. Appendix). Small
220 differences may be observed due to the different strategies adopted by the two modes (*i.e.*,
221 discrete ordinates for DART-FT, Bi-directional Monte Carlo for DART-Lux), and also due to

the approximation of turbid volumes by clouds of facets. These differences are supposed to be negligeable compared to the differences caused by the canopy structure.

2.5. Simulated structural complexity

Three structurally different forest abstractions were considered for this study (Figure 3):

1. 3D mock-ups: derived from airborne LiDAR data, with classified sun- and shade-adapted cells as explained in the two previous sections.
2. 1D mock-ups: horizontally homogenized 3D mock-ups having the same heights and vertical profiles of sun- and shade-adapted leaf area density and wood area density but missing the forest horizontal heterogeneity.
3. 0D mock-ups: horizontally and vertically homogenized mock-ups having the mean height of the original 3D canopies, shade-adapted leaves homogeneously distributed in the mock-up bottom half, sun-adapted leaves homogeneously distributed in the mock-up top half, and woody elements homogeneously distributed within the entire scene. Compared to 3D forest mock-ups, 0D mock-ups miss the forest horizontal and vertical heterogeneity, including the simplifying assumption that all sun-adapted leaves are located at the top and all the shade-adapted leaves are located at the bottom of the canopy.

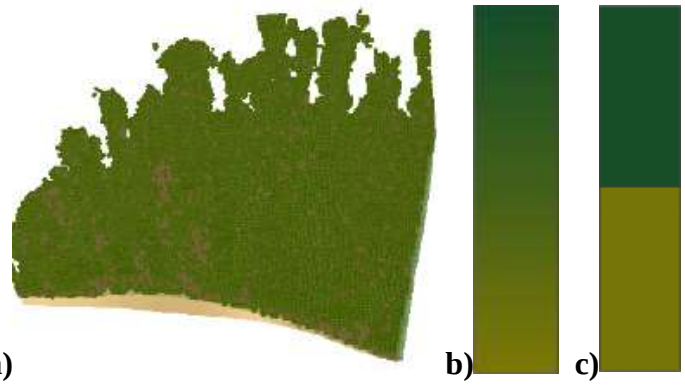

Figure 3: The three types of scene abstractions: a) 3D, b) 1D, c) 0D (top: sun-adapted, bottom: shade-adapted leaves)

2.6. Simulated SIF products

SIF nadir images of a high spectral resolution, from 0.15 nm to 4 nm (Table 5), were simulated with DART-Lux. DART-FT was used to simulate the PAR and SIF radiative budget with a

lower spectral resolution ([400-640 nm] at 20 nm resolution, [640-850] at 10 nm resolution) and 40 discrete directions, in order to limit computational demands.

Table 5. The 372 spectral bands of DART-Lux simulations. They over-sample the O_2B (~687nm) and O_2A (~760nm) oxygen absorption bands, and under-sample the [400-640nm] band (no SIF emission)

Spectral interval (nm)	Spectral resolution (nm)	Number of spectral bands
400-640	4	60
640-641.5	1.5	1
641.5-686.5	1	45
686.5-694	0.15	50
694-694.5	0.5	1
694.5-759.5	1	65
759.5-770	0.15	70
770-770.5	0.5	1
770.5-848.5	1	78
848.5-850	1.5	1

The influence of the canopy 3D architectures on 3D SIF emissions was assessed by comparing the DART-FT RB fluxes (*i.e.*, intercepted, scattered, absorbed and emitted PAR and total SIF radiation) per voxel in the simulated 3D, 1D and 0D mock-ups. Here, the PAR absorbed by leaves ($W.m^{-2}$) informs us on $APAR_{green}$ (the 1st process). $SIF_{emitted}$ ($W.m^{-2}$) is the sum of PSI and PSII emissions by adaxial and abaxial sides of all leaves in the canopy. It depends on the directionality and intensity of the incident PAR relative to leaf orientation, and therefore on $APAR_{green}$ and the local leaf physiology (*e.g.*, leaf sun and shade adaptations). SIF emission yield informs us on the 2nd process. It is defined as:

$$\text{SIF emission yield} = \frac{\text{SIF}_{\text{emitted}}}{\text{APAR}_{\text{green}}}. \quad (1)$$

Since satellite and airborne spectrometers only measure SIF radiation that exits a canopy, the 3rd process is investigated through the so-called SIF escape factor$_{hemi}$:

$$\text{SIF escape factor}_{hemi} = \frac{\text{SIF}_{\text{exitance}}}{\text{SIF}_{\text{emitted}}} \quad (2)$$

where $SIF_{exitance}$ is the total SIF radiation exiting the top of the canopy in all directions of the upper hemisphere. SIF escape $factor_{hemi}$ was computed for the chlorophyll fluorescence peaks located at 640 – 700 nm and 700 – 850 nm spectral regions.

SIF sensors generally measure from a unique viewing direction. Hence, the directional SIF nadir escape factor was also studied:

$$\text{SIF escape factor}_{nadir} = \frac{\pi.\,\text{SIF}_{nadir\ radiance}}{\text{SIF}_{\text{emitted}}} \quad (3)$$

SIF escape $factor_{nadir}$ was also computed for the chlorophyll fluorescence peaks located at 640 – 700 nm and 700 – 850 nm spectral regions.

Finally, the combination of the 2nd and the 3rd processes was in the case of a nadir observation evaluated with the SIF nadir yield (sr^{-1}) (van der Tol et al., 2019):

$$\text{SIF nadir yield} = \frac{\text{SIF}_{\text{nadir radiance}}}{\text{APAR}_{\text{green}}} \quad (4)$$

where $SIF_{\text{nadir radiance}}$ is a SIF flux ($W.m^{-2}.sr^{-1}$), that is for example recorded by an optical remote sensing sensor in the nadir viewing direction.

2.7. Canopy structure error assessment

The impact of forest architecture on diurnal SIF emission and nadir observation was assessed as the relative errors made on SIF quantities that are simulated with mock-ups (*i.e.*, 1D, 0D) with simplified architecture, taking the quantities simulated with the 3D mock-ups as reference.

The influence of forest 3D structure on SIF observation was assessed by comparing the DART-Lux top-of-canopy (TOC) nadir SIF radiance L_v (PSI, PSII and total), of the 3D, 1D and 0D mock-ups of the eight forest sites simulated. Two types of relative errors were computed:

- Per spectral band for a specific time (*e.g.*, 12.00 local time), by computing the relative errors $\boldsymbol{\varepsilon_{SIF,L_v,iD-3D}(\lambda)}$ where $\boldsymbol{i} \in \{\mathbf{0}, \mathbf{1}\}$:

$$\varepsilon_{SIF,L_v,iD-3D}(\lambda) = 100\% \times \frac{SIF_{radiance,iD}(\lambda) - SIF_{radiance,3D}(\lambda)}{SIF_{radiance,3D}(\lambda)} \quad (5)$$

- Per hour from 7.00 to 19.00, by computing mean absolute relative errors (MARE) for the two 640 – 700 nm and 700 – 850 nm spectral regions:

$$MARE_{SIF,L_v,1D-3D}(t) = \frac{1}{\sum_i \Delta\lambda_i} . \sum_i \frac{|SIF_{radiance,1D}(t,\lambda) - SIF_{radiance,3D}(t,\lambda)|}{SIF_{radiance,3D}(t,\lambda)} . \Delta\lambda_i \quad (6)$$

Using 3D plots as reference, the influence of canopy architecture was also assessed for:

- Nadir reflectance ρ:relative errors $\varepsilon_{\rho,0D\text{-}3D}(\lambda)$and $\varepsilon_{\rho,1D\text{-}3D}(\lambda)$ of 0D and 1D plots, as well as $MARE_{\rho,1D\text{-}3D}(t)$ of 1D plots.

- $APAR_{green}$: relative error $\varepsilon_{APAR,1D-3D}(t)$ of 1D plots.

- SIF emission yield: relative error $\varepsilon_{SIF.EY,1D-3D}(t)$ of 1D plots.

- $SIF_{emitted}$: relative error $\varepsilon_{SIF.em,1D-3D}(t)$ of 1D plots.

-SIF escape $factor_{hemi}$ and SIF escape $factor_{nadir}$: relative errors $\varepsilon_{SIF.EF,1D-3D}(t)$ of 1D plots at 640 – 700 nm and 700 – 850 nm spectral regions.

- SIF nadir yield: relative errors $\varepsilon_{SIF.NY,1D-3D}(t)$ of 1D plots at 640 - 700 nm and 700 - 850 nm.

with relative error for a given quantity Q equal to $\varepsilon_{Q,1D-3D}(t) = 100\% \times \frac{Q_{1D}(t) - Q_{3D}(t)}{Q_{3D}(t)}$.

2.8. Influence of canopy wood on SIF emission and measurements

Although they do not intrinsically emit fluorescence, woody elements impact the RB and SIF observations through their interaction with PAR and SIF. They give rise to two major effects. i) Shading effect: woody elements shade foliar elements, which lowers leaf irradiance and subsequently SIF emission. ii) Blocking effect: woody elements intercept the emitted SIF radiation, preventing it from escaping the canopy. These two effects are not independent, due to sky radiation and multiple scattering and re-absorption mechanisms in the canopy. For example, the same woody element can shade a leaf element and block its SIF radiation.

DART simulations were used to quantify the influence of woody elements on SIF observation, and to separate the shading and blocking effects of woody elements for the CM1 and LM2 sites. For that, theoretical "no wood" (NW) scenes were constructed by removing cells corresponding to woody elements from the original "with wood" 3D mock-ups (W). It allowed us to compare

the DART-Lux top-of-canopy (TOC) nadir SIF radiance (PSI, PSII and total) of the (W) and (NW) abstractions, and to compute two types of relative error:

- Per spectral band for a specific time (*e.g.*, 12.00 local time):

$$\varepsilon_{SIF,L_v,NW-W}(\lambda) = 100\% \times \frac{SIF_{radiance,NW}(\lambda) - SIF_{radiance,W}(\lambda)}{SIF_{radiance,W}(\lambda)} \quad (7)$$

- Per hour from 7.00 to 19.00, by computing mean absolute relative errors for the 640 – 700 nm and 700 – 850 nm spectral regions:

$$MARE_{SIF,L_v,NW-W}(t) = \frac{1}{\sum_i \Delta\lambda_i} . \sum_i \frac{|SIF_{radiance,NW}(t,\lambda) - SIF_{radiance,W}(t,\lambda)|}{SIF_{radiance,W}(t,\lambda)} . \Delta\lambda_i \quad (8)$$

Using W plots as reference, the influence of woody elements was assessed for:

- $\mathrm{APAR}_{\mathrm{green}}$ (shading effect): relative error $\varepsilon_{APAR,NW-W}(t)$ NW.

- SIF nadir escape factor $\mathrm{SIF}_{nadir\ EF}$ (blocking effect): relative error $\varepsilon_{SIF.NEF,NW-W}(t)$ of NW plots, where:

$$\mathrm{SIF}_{nadir\ EF} = \frac{\pi\ .\ \mathrm{SIF}_{\mathrm{nadir\ radiance}}}{\mathrm{SIF}_{\mathrm{emitted}}} \quad (9)$$

With the relative error for a given quantity Q equal to:

$$\varepsilon_{Q,NW-W}(t) = 100\% \times \frac{Q_{NW}\ (t) - Q_W(t)}{Q_W(t)} \quad (10)$$

3. Results

3.1. General influence of forest abstractions on SIF nadir observations

Figure 4 shows the PSI, PSII and total SIF nadir radiance of the 8 forest plots simulated with 3D, 1D and 0D mock-ups at 12.00 (SZA = 21.050°, SAA = 47.256°). $\varepsilon_{SIF,L_v,0D-3D}(\lambda)$ and $\varepsilon_{SIF,L_v,1D-3D}(\lambda)$ quantify the relative errors associated with the 0D and 1D forest plots. For all plots, the 1D mock-ups give the largest nadir total SIF, PSI and PSII radiance. $\varepsilon_{SIF,L_v,1D-3D}$ illustrates the influence of the forest horizontal heterogeneity on radiation propagation in forest, since the canopy horizontal heterogeneity is the only difference between 3D and 1D mock-ups. These larger values of 1D SIF radiance can be explained by the fact that the top layers of 1D

330 plots intercept more radiation than the top layers of 3D plots (i.e., clumping effect), which gives
331 rise to larger SIF emission by canopy layers that tend to contribute most to the canopy SIF
332 radiance. Also, the ground is more visible in 3D plots than 1D plots, whereas the ground has no
333 SIF emission. The order of magnitude of the difference between the radiance of 1D and 3D
334 mockups is similar for all investigated forest sites.

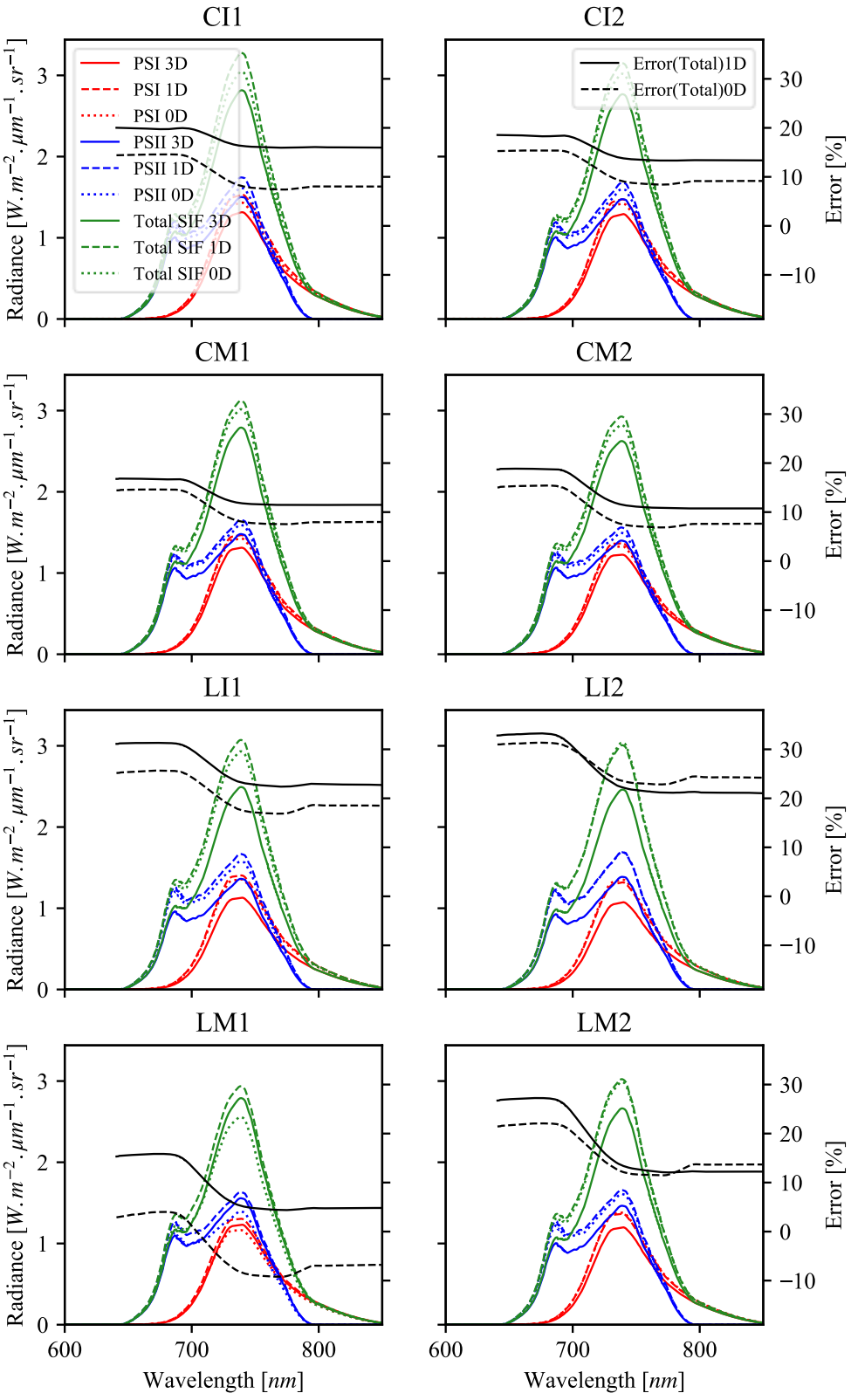

Figure 4. PSI, PSII and total SIF nadir radiance of the eight sites simulated with 3D, 1D and 0D abstractions, at 12.00 local time (SZA = 21.050°, SAA = 47.256°).

SIF radiance values of 0D and 1D forest mock-ups differ due to differences in the leaf and wood vertical distributions, which vary greatly among the sites (except for LI2 and LM2). In general, nadir SIF radiance relative differences $\varepsilon_{SIF,L_v,0D-1D}(\lambda)$ between 0D and 1D plots are much smaller than $\varepsilon_{SIF,L_v,1D-3D}(\lambda)$ between 1D and 3D plots, except for LM1.It means that forest horizontal heterogeneity has a larger influence on SIF radiance than forest vertical heterogeneity. SIF radiance was always smaller for 0D mock-ups than for 1D mockups. This is mostly explained by the homogenized vertical distribution of both foliar and woody elements in the 0D abstractions compared to 1D abstractions. For example, in CI1, CI2, CM1 and CM2, leaf density is higher in upper canopy layers (Figure 14), foliar homogenization increases the density of foliar elements in the canopy bottom layers, which increases the canopy shading and blocking effects. For LI2, the situation is different because leaf density is highest in the lower canopy layers. Therefore, foliar homogenization increases leaf density in the canopy upper layers, which decreases the canopy shading and blocking effects. These trends are also influenced by the vertical distribution of woody elements.

The relative difference $\varepsilon_{SIF,L_v,0D-3D}(\lambda)$ between the radiance of 0D and 3D mock-ups is driven by horizontal and vertical heterogeneity. The inequality $\varepsilon_{SIF,L_v,0D-3D}(\lambda) < \varepsilon_{SIF,L_v,1D-3D}(\lambda)$ indicates that vertical and horizontal heterogeneities have an opposite effect on canopy SIF radiance in our simulations. While the horizontal heterogeneity tends to decrease canopy SIF nadir radiance, the vertical heterogeneity tends to increase it. LM1 is an exception. Its 0D SIF radiance is lower than its 3D SIF radiance in the NIR domain. It means that its vertical heterogeneity imposes a larger influence on SIF nadir radiance than its horizontal heterogeneity, which is consistent with the fact that LM1 is the only plot where the density of woody and foliar elements is very dense in the lower canopy layers.

Figure 5 shows the diurnal evolution of $MARE_{SIF,L_v,1D-3D}(t)$ (*i.e.*, relative error of total nadir SIF radiance of 1D plots compared to 3D plots) at 640 - 700 nm and 700 - 850 nm. This quantity is mostly influenced by the forest horizontal heterogeneity. It appears symmetrically distributed between the morning and the afternoon hours, with a dip appearing always at local noon. It is the largest around 8.00 and 18.00, reaching up to 55%, and the smallest at 13.00 (local solar noon), with values between 10% and 20%. It is usually larger at 640 - 700 nm than at 700 - 850 nm, where shading effects are dampened by prevailing multiple scattering events. This diurnal variation can be explained by the shadow effects associated with changing solar zenith angle

and associated variability in the proportions of direct sun and diffuse atmospheric radiation. In the early morning, it starts increasing because shadow effects are increasing due to the increase of the direct sun proportion in total irradiance. Later in the morning, it starts decreasing because shadow effects decrease due to the decrease of solar zenith angle, reaching a minimum at solar noon. A symmetrical behavior starts in the second half of the day.

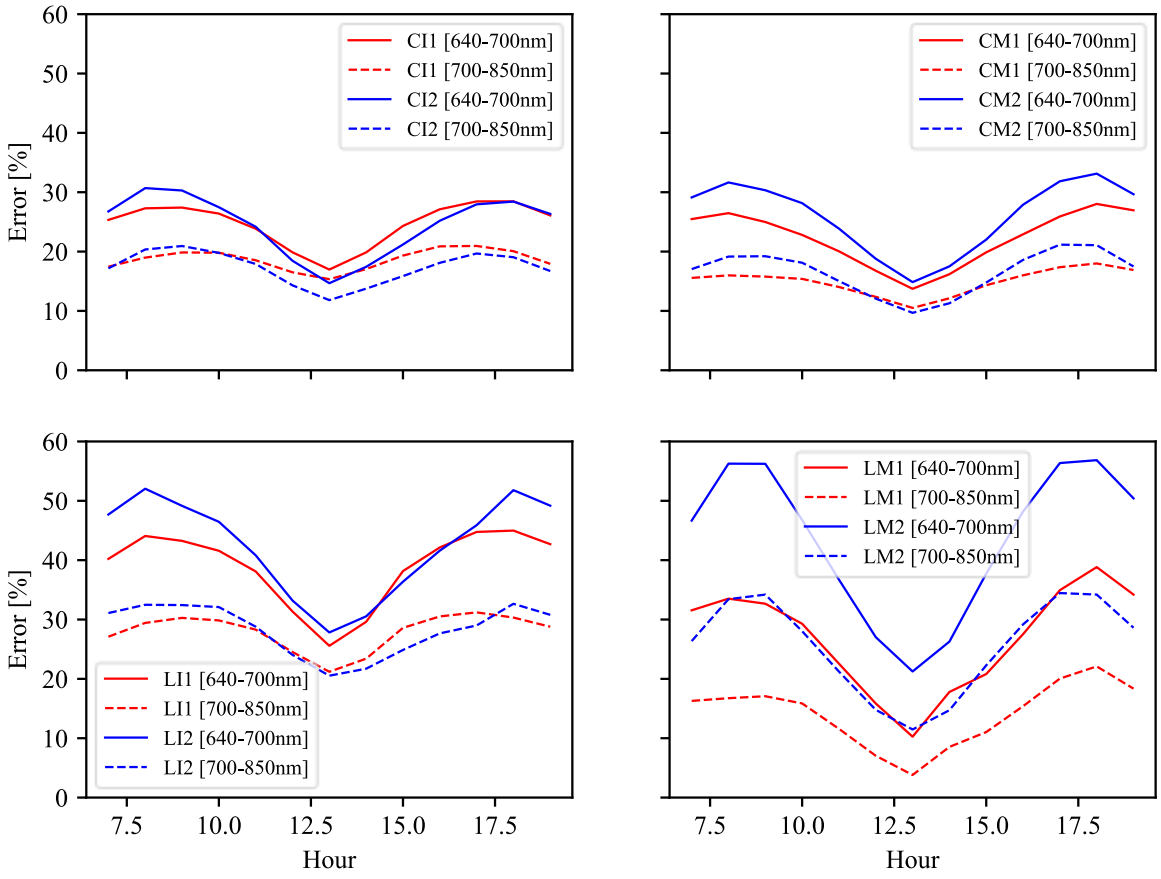

Figure 5. Diurnal evolution of the total nadir SIF radiance relative error $MARE_{SIF,L,1D-3D}(t)$ between 1D and 3D mock-ups at 640 – 700 nm and 700 – 850 nm.

Figure 6 shows the canopy nadir reflectance of the 8 forest plots simulated with 3D, 1D and 0D mock-ups at 12.00 (SZA = 21.050°, SAA = 47.256°). $\varepsilon_{\rho,0D-3D}(\lambda)$ and $\varepsilon_{\rho,1D-3D}(\lambda)$ quantify the of 0D and 1D abstractions compared to 3D abstraction. All curves have the expected local spectral peak around the O_2-A absorption band at 760nm. As for the SIF radiance (Figure 4), the total reflectance of 3D plots is the smallest compared to the 1D and 0D plots, except for LM1 where the 0D plot has a slightly lower reflectance than the 3D plot above 700nm.

Therefore, as for SIF radiance, the horizontal heterogeneity tends to decrease the nadir reflectance.

The influence of the vertical heterogeneity of the plots on their reflectance is not as clear as for SIF radiance. By contrast to the relative errors on the SIF radiance, the relative errors on the total reflectance of the 1D and 0D forest plots are similar. This stresses two points. 1) As for SIF, the forest vertical heterogeneity plays a lesser role than the forest horizontal heterogeneity. 2) The vertical heterogeneity plays a larger role for canopy SIF radiance than for canopy radiance that contains radiance due to the scattering of solar radiation. Also, these relative errors tend to higher for wavelengths under 700nm. Indeed, the 1D and 0D abstractions of the forest cover neglect the shadow effects due to direct and diffuse radiation and canopy structure. Multiple scattering being smaller at wavelengths lower than 700nm, shadowing effects are larger in these wavelengths. The diurnal evolutions of the relative error $MARE_{\rho,1D-3D}(t)$ in nadir reflectance of 1D plots at 640-700 nm and 700-850 nm (Figure 7) have shapes and orders of magnitude similar to those of SIF radiance $MARE_{SIF,L,1D-3D}$ (Figure 5), except for LI2 at 640 - 700nm, where the relative error is higher for SIF radiance.

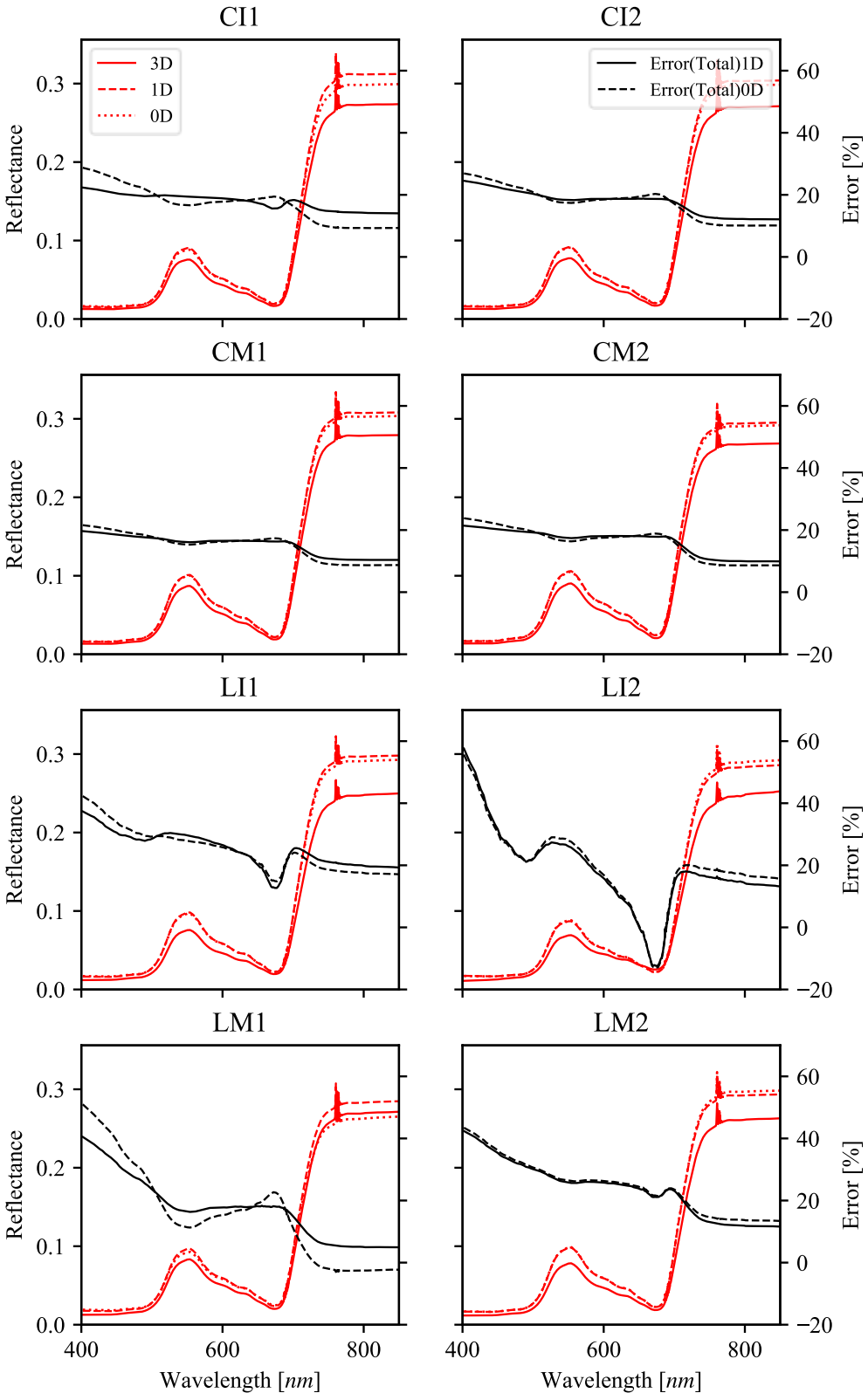

Figure 6: Canopy nadir reflectance of the eight study sites simulated with 3D, 1D and 0D mock-ups, at 12.00 local time (SZA = 21.050°, SAA = 47.256°). $\varepsilon_{\rho,1D-3D}(\lambda)$

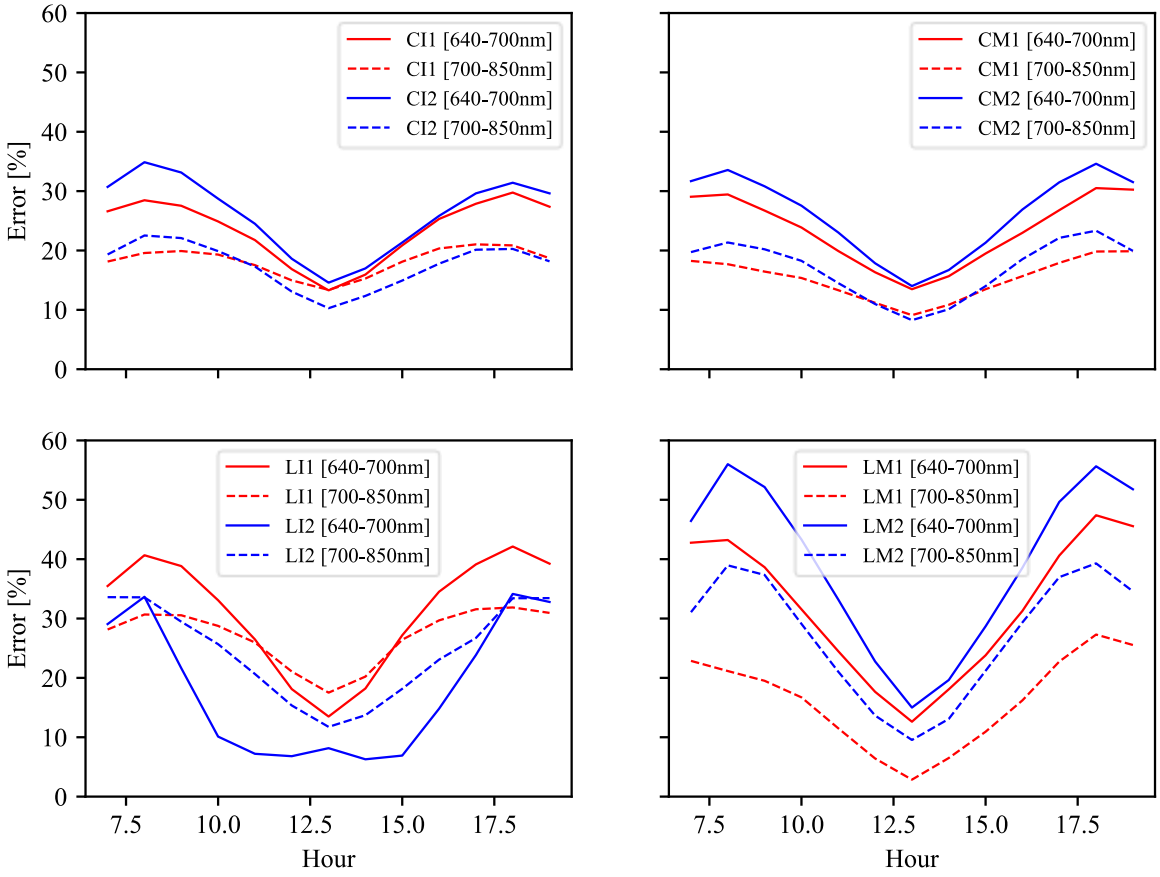

Figure 7: Diurnal evolution of canopy nadir reflectance relative error $MARE_{\rho,1D-3D}$ at 640-700 nm and 700-850 nm due to differences in horizontal heterogeneity in 1D and 3D mock-ups.

3.2. Impact of forest 3D structure on $APAR_{green}$ (1st process)

Figure 8 shows the diurnal PAR absorbed by green leaves ($APAR_{green}$) in the eight 3D and 1D forest mock-ups, and their associated relative error $\varepsilon_{APAR,1D-3D}(t)$. The 3D mock-ups have smaller $APAR_{green}$ than the 1D mock-ups. This is consistent with the larger reflectance of 1D mock-ups compared to the 3D mock-ups, due to the horizontal heterogeneity of the forest plots. $\varepsilon_{APAR,1D-3D}(t)$ is usually smaller than 5%, with a maximum of 10% for LI2 before noon. It is smaller than the relative difference of nadir SIF radiance between 3D and 1D forest abstractions (Figure 5). This indicates that even though the $APAR_{green}$ diurnal changes play an important role, they are not the only cause responsible for the relative difference in the nadir SIF radiance.

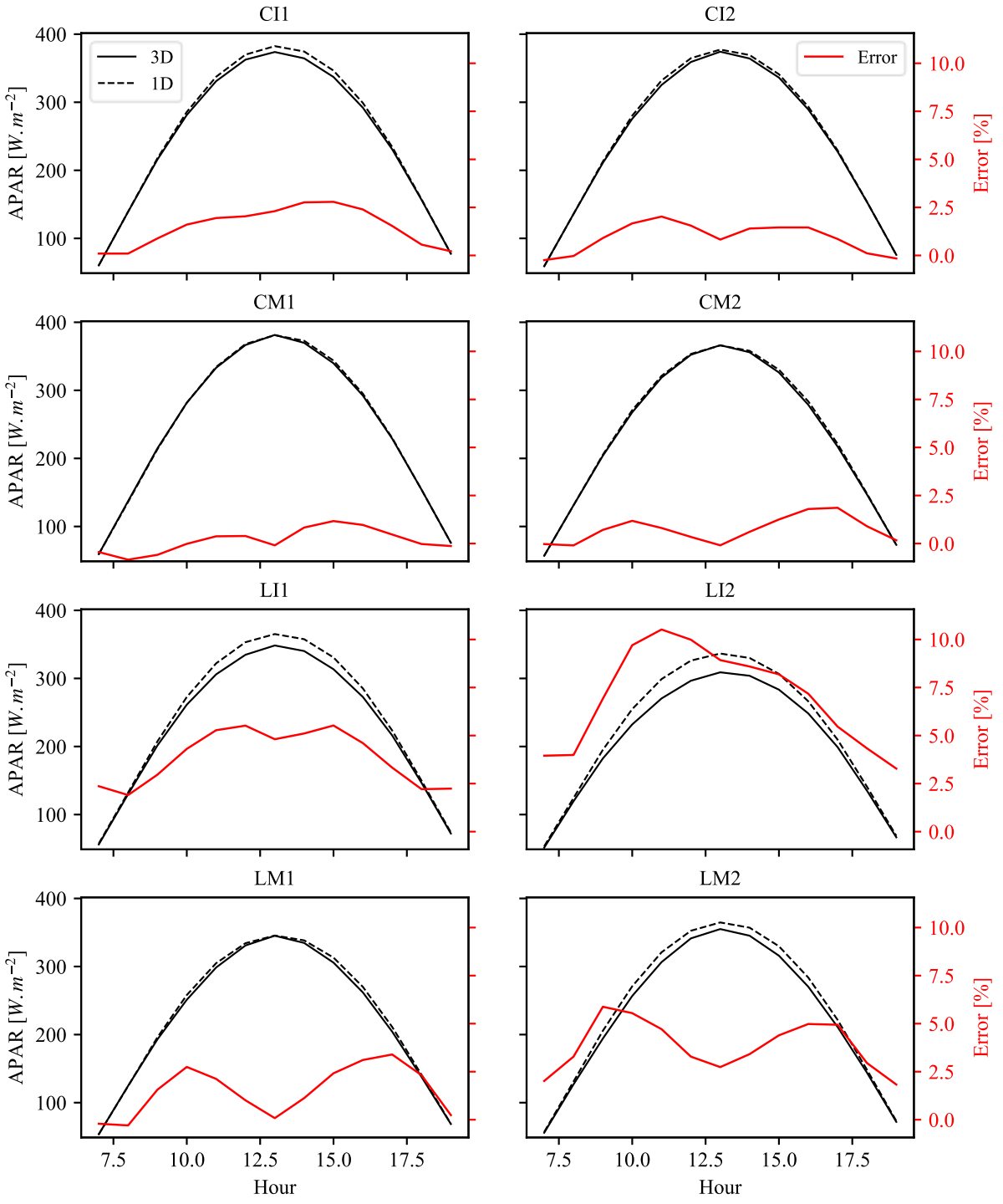

Figure 8. Diurnal PAR absorbed by green leaves ($APAR_{green}$) in 3D and 1D forest abstractions of the eight study sites, and their associated relative error $\varepsilon_{APAR,1D-3D}(t)$ triggered by changes in horizontal heterogeneity of the forest abstractions.

3.3. Impact of forest 3D structure on leaf SIF emission yield (2nd process)

Figure 9 shows the diurnal total SIF emission yield for 3D and 1D mock-ups and the associated diurnal relative error $\varepsilon_{SIF.EY,1D-3D}(t)$ due to horizontal heterogeneity differences. Relative errors are similar and small for all plots. They reveal that in our simulations the impact of forest 3D architecture on SIF emission yield in our simulations is of a less importance. The almost constant diurnal response due to our modeling assumption of constant leaf SIF properties throughout the day.

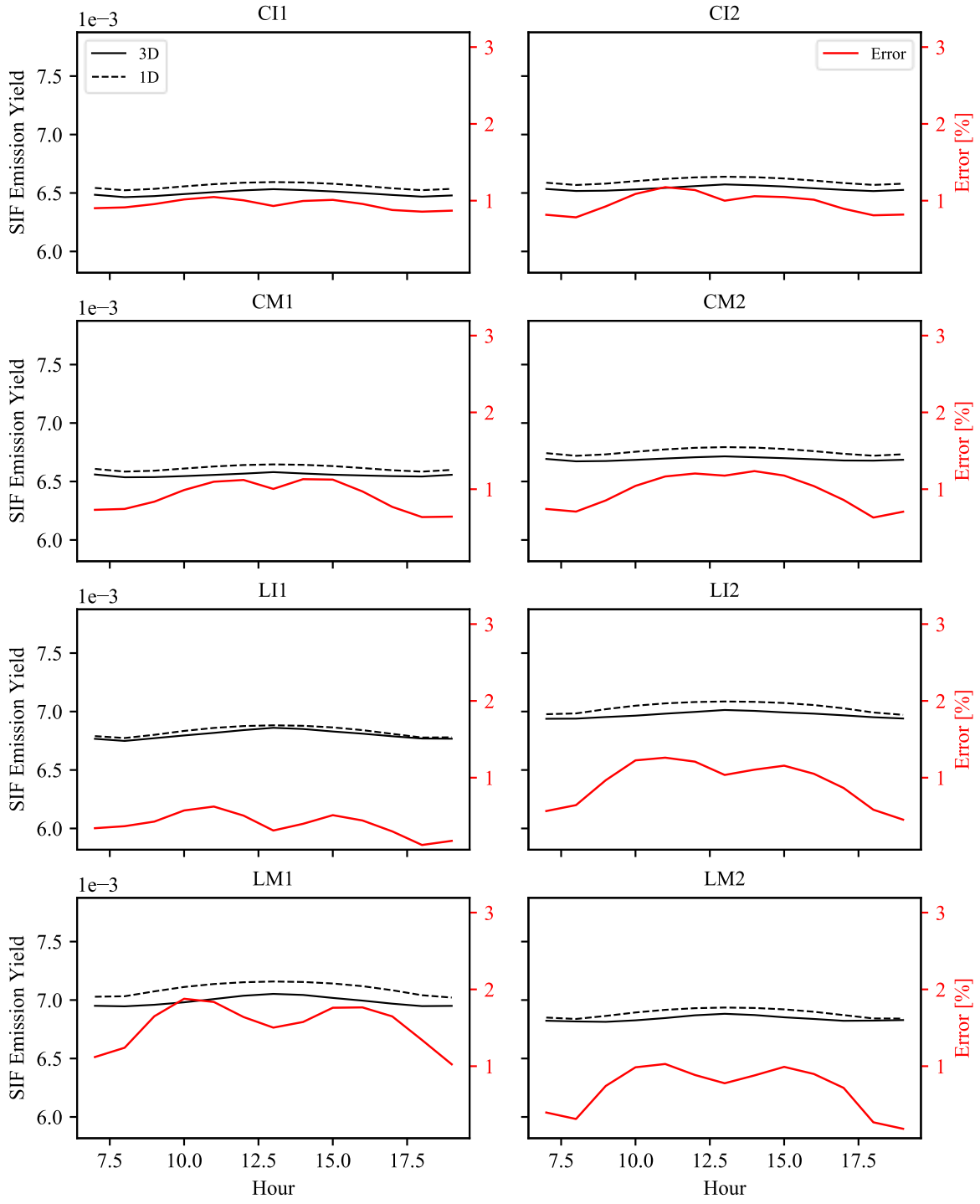

Figure 9. Diurnal SIF emission yield of the 3D and 1D forest mock-ups and relative errors $\varepsilon_{SIF.EY,1D-3D}(t)$

Since SIF emission yield in our simulations is hardly affected by the forest 3D architecture, the diurnal behavior of the DART-FT simulated leaf SIF emission (Figure 10) is understandably very similar to that of $APAR_{green}$ (Figure 8). The relative error $\varepsilon_{SIF.em,1D-3D}(t)$ computed

441 between the 3D and 1D forest abstractions (Figure 10) gathers the combined errors related to
442 both the 1st and the 2nd processes, without being a simple addition of their relative errors.
443 Figure 11 plots the vertical profiles of LAI, and SIF emission in 3D and 1D plots. The LAI of
444 a layer i located between $[i\ m, (i+1)\ m]$ is the total foliar area of this layer divided by the
445 scene area. It shows that the overestimation of the SIF emission in 1D plots compared to 3D
446 plots mainly occurs in the canopy top layers, *i.e.*, $\mathrm{SIF}_{\mathrm{emitted,1D}} > \mathrm{SIF}_{\mathrm{emitted,3D}}$ in these layers.
447 Also, SIF emission is underestimated in the lower layers of 1D plots. Indeed, in 3D forest mock-
448 ups, the forest horizontal heterogeneity leads to better illumination of the lower layers.
449

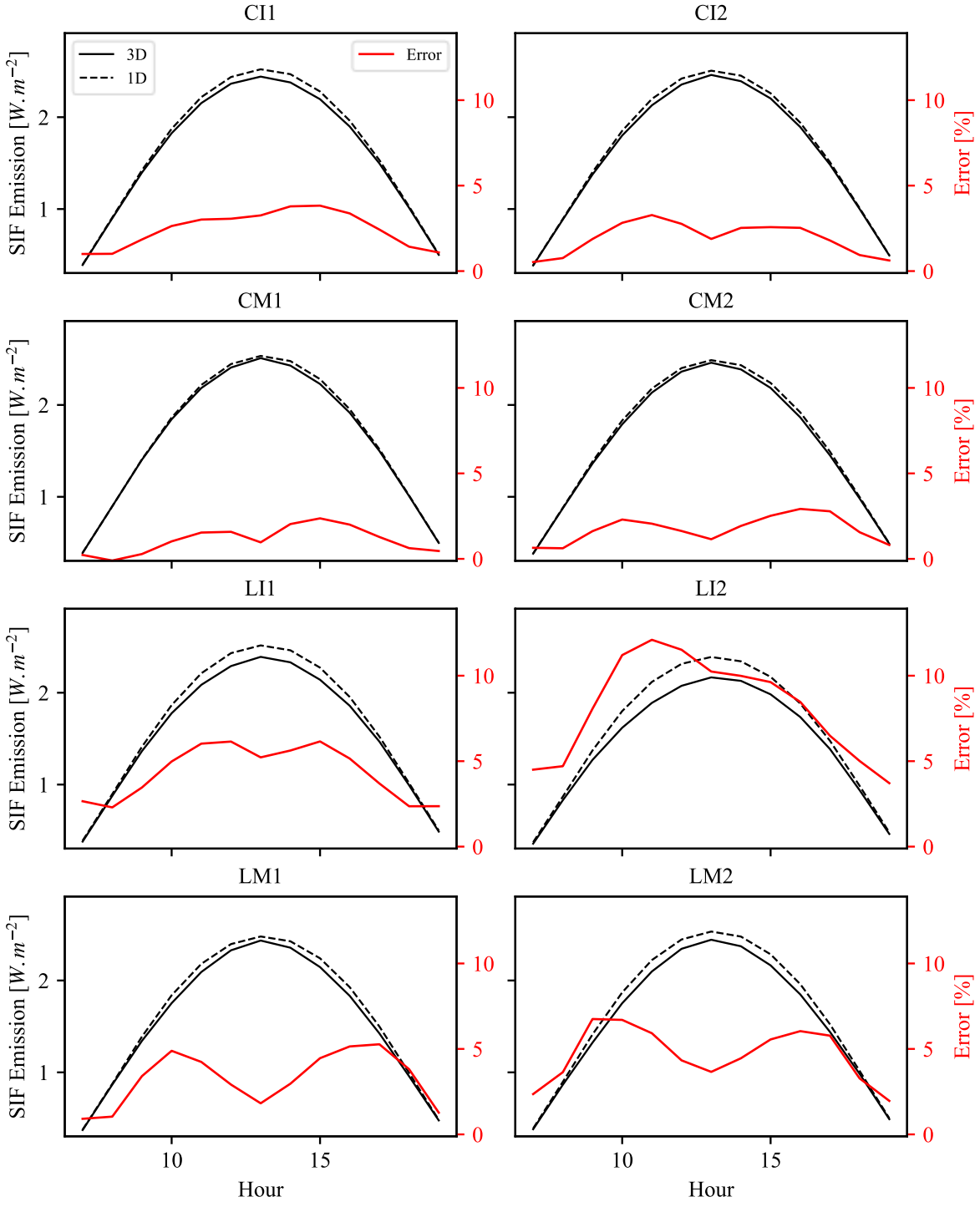

Figure 10. Diurnal leaf SIF emissions for the 3D and 1D forest abstractions and their associated relative errors $\varepsilon_{SIF.em,1D-3D}(t)$.

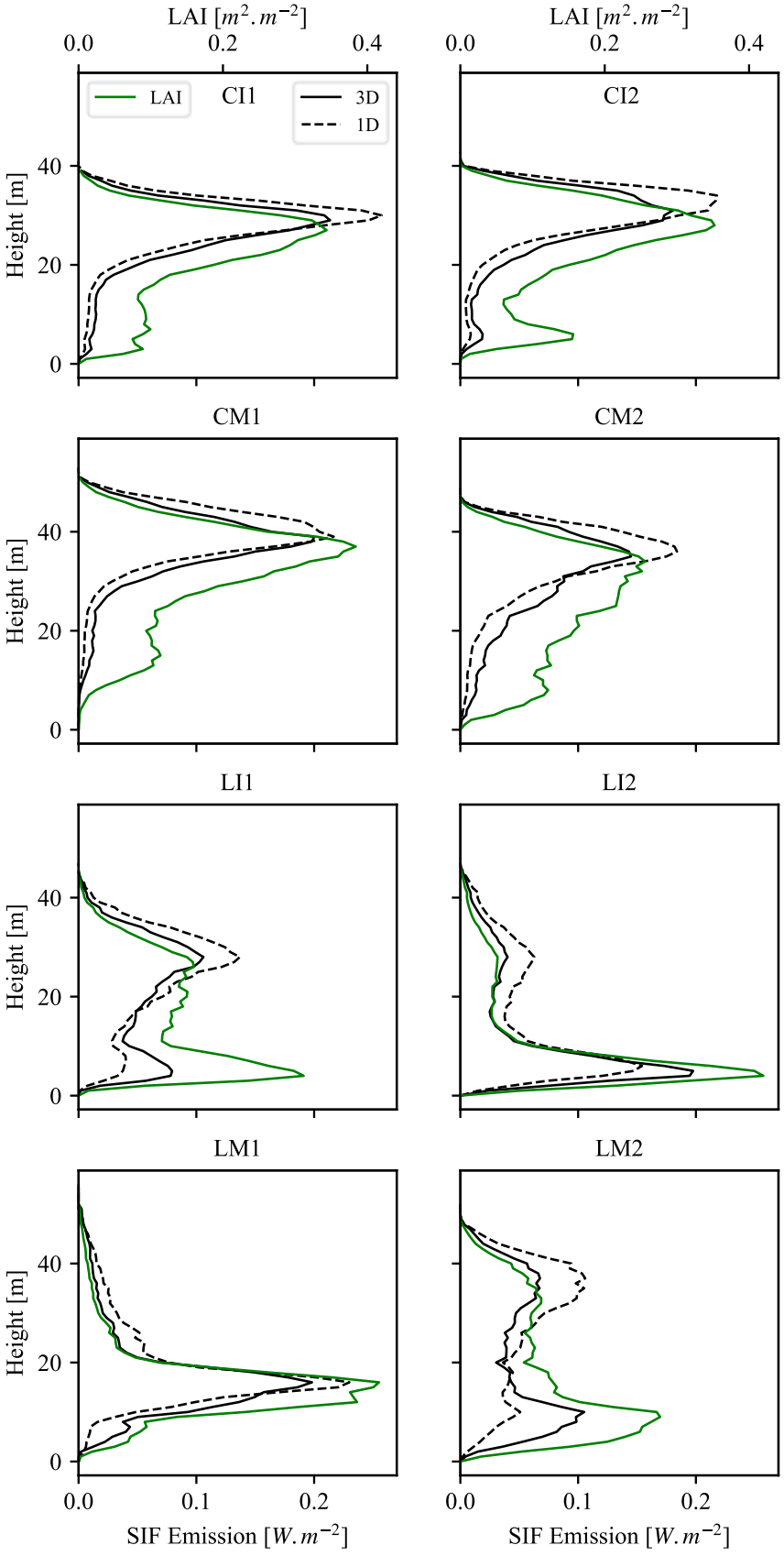

Figure 11. Vertical profiles of LAI and leaf SIF emission at 12.00 (local time).

3.4. Impact of forest 3D structure on SIF escape factor (3rd process)

Figure 12 and Figure 13 show the diurnal SIF escape factor$_{hemi}$ and SIF escape factor$_{nadir}$ of 3D and 1D plots at 640 - 700 nm and 700 nm - 850 nm, and their relative errors $\varepsilon_{SIF.EF,1D-3D}(t)$ and $\varepsilon_{SIF.EFnadir,1D-3D}(t)$ are larger (*e.g.*, > 50% for LM2) than for APAR$_{green}$ (Figure 8) and leaf SIF emission (Figure 10). Therefore, the 3rd process is more affected by forest 3D structure than the first two processes. The SIF escape factor is systematically overestimated in 1D plots. It is larger at 700 nm - 850 nm than at 640 - 700 nm, due to more important multiple scattering mechanisms, which results in lower relative errors at 700 nm - 850 nm than at 640 - 700 nm.

The SIF photons that cannot escape the canopy are absorbed by the canopy elements (i.e., leaves, woody elements, ground). The overestimation of the SIF escape factor of 1D plots compared to 3D plots is also reflected by a higher absorption of SIF photons in 3D plots (Table 6, Table 7). We can note that the ground absorption is greatly underestimated in 1D forest abstractions. Again, this is explained by the forest horizontal heterogeneity.

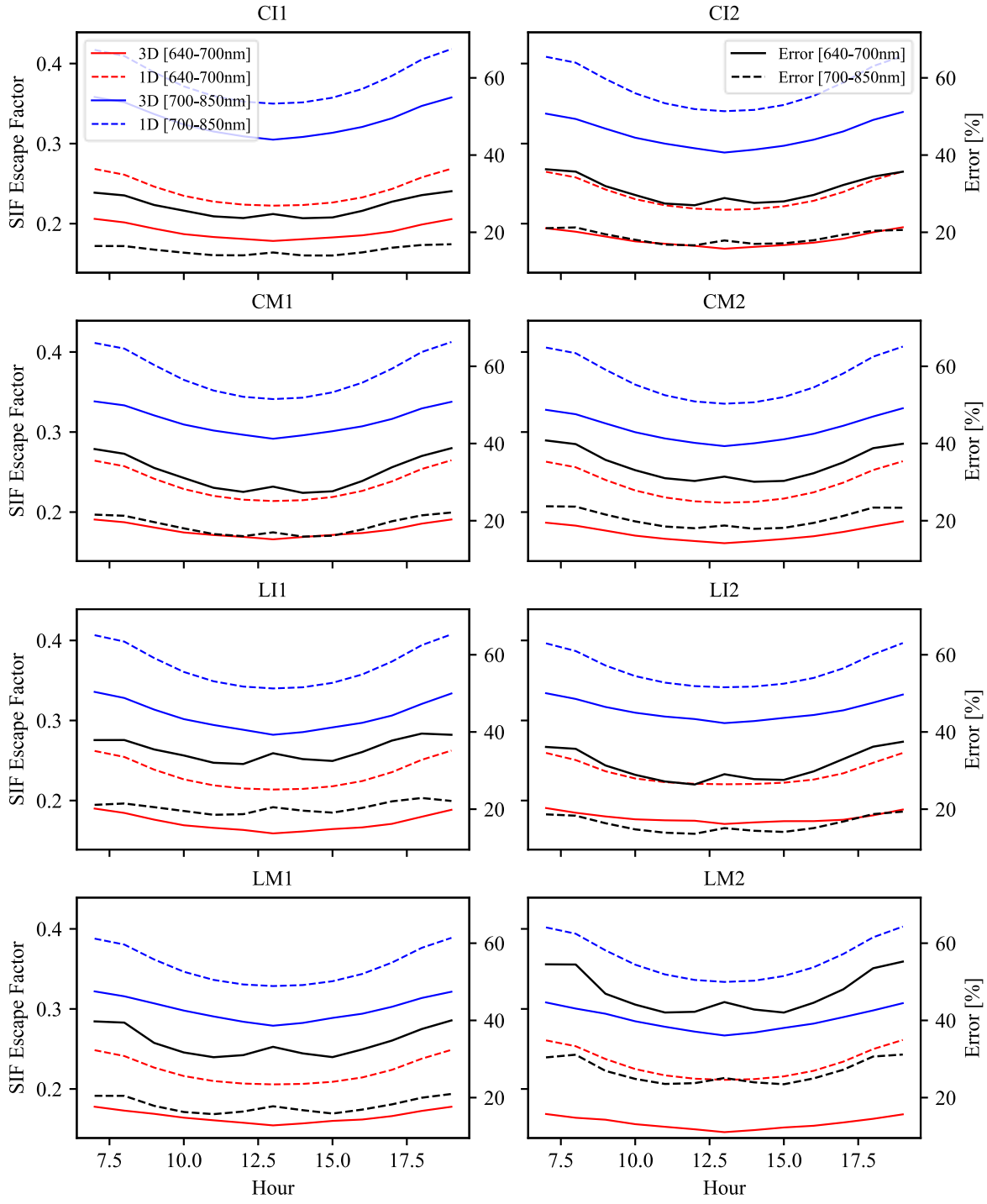

Figure 12. Diurnal SIF escape factor$_{hemi}$ of the 3D and 1D plots and their associated relative errors.

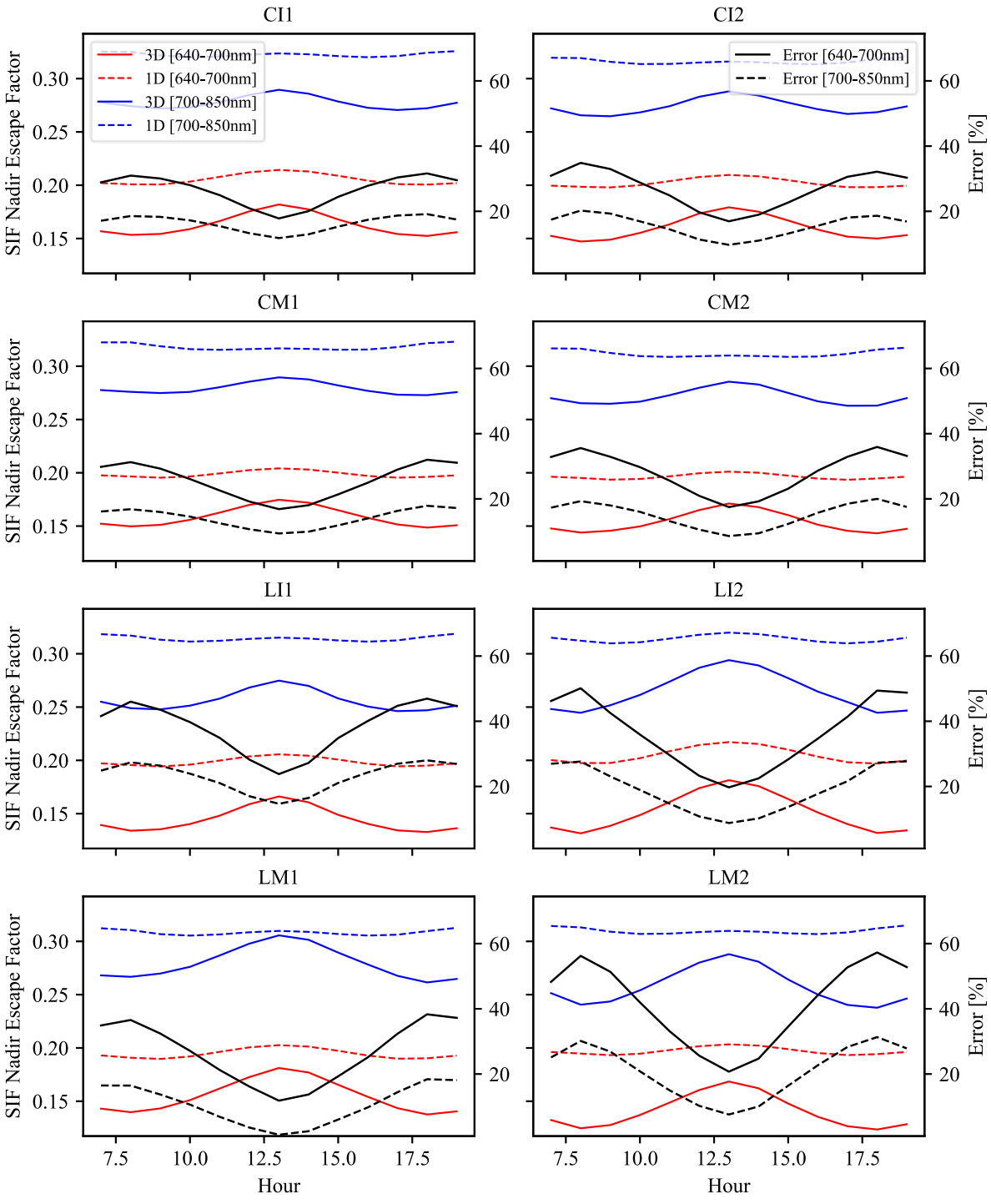

Figure 13: Diurnal SIF escape factor$_{nadir}$ of the 3D and 1D plots and their associated relative errors.

Figure 14 shows the vertical profiles of LAI, woody elements (defined similarly as the vertical profile of LAI), and SIF absorption in 3D and 1D plots. The vertical profiles of SIF absorption

478 show that in 1D forest abstractions, absorption is overestimated in the top layers and
479 underestimated in the bottom layers as for the leaf SIF emission profiles (Figure 11).

480

481 Table 6. SIF absorption by the ground and vegetation (leaves and wood) (640-700nm) at 12pm

Plot	CI1	CI2	CM1	CM2	LI1	LI2	LM1	LM2
Fraction of emitted SIF absorbed by "Ground" (3D)	0,0310	0,0290	0,0230	0,0272	0,0463	0,0704	0,0486	0,0449
Fraction of emitted SIF absorbed by "Ground" (1D)	0,0216	0,0180	0,0130	0,0160	0,0301	0,0584	0,0329	0,0274
Relative difference (%)	-30,28	-38,19	-43,40	-41,38	-35,14	-17,12	-32,44	-38,97
Fraction of emitted SIF absorbed by "Leaves + Wood" (3D)	0,7765	0,7838	0,7903	0,7912	0,7757	0,7352	0,7636	0,7843
Fraction of emitted SIF absorbed by "Leaves + Wood" (1D)	0,7512	0,7545	0,7616	0,7613	0,7461	0,7073	0,7462	0,7492
Relative difference (%)	-3,26	-3,74	-3,63	-3,78	-3,81	-3,79	-2,28	-4,47
Absorption fraction (3D)	0,8075	0,8129	0,8133	0,8184	0,8220	0,8056	0,8123	0,8291
Absorption fraction (1D)	0,7728	0,7725	0,7746	0,7772	0,7762	0,7657	0,7791	0,7766
Relative difference (%)	-4,30	-4,97	-4,76	-5,03	-5,57	-4,95	-4,09	-6,34

482

483 Table 7. SIF absorption by the ground and vegetation (leaves and wood) (700-850nm) at 12pm.

Plot	CI1	CI2	CM1	CM2	LI1	LI2	LM1	LM2
Fraction of emitted SIF absorbed by "Ground" (3D)	0,0905	0,0842	0,0683	0,0768	0,1249	0,1741	0,1282	0,1249
Fraction of emitted SIF absorbed by "Ground" (1D)	0,0716	0,0593	0,0440	0,0502	0,0941	0,1640	0,0952	0,0887
Relative difference (%)	-20,96	-29,52	-35,50	-34,62	-24,68	-5,78	-25,71	-28,95
Fraction of emitted SIF absorbed by "Leaves + Wood" (3D)	0,6194	0,6369	0,6543	0,6600	0,6062	0,5265	0,5897	0,6185
Fraction of emitted SIF absorbed by "Leaves + Wood" (1D)	0,6133	0,6257	0,6453	0,6482	0,5991	0,5098	0,6037	0,6057
Relative difference (%)	-0,98	-1,77	-1,39	-1,79	-1,16	-3,19	2,38	-2,08
Absorption fraction (3D)	0,7099	0,7211	0,7226	0,7369	0,7311	0,7006	0,7179	0,7434
Absorption fraction (1D)	0,6849	0,6850	0,6893	0,6985	0,6932	0,6738	0,6989	0,6944
Relative difference (%)	-3,53	-5,01	-4,61	-5,21	-5,18	-3,83	-2,64	-6,59

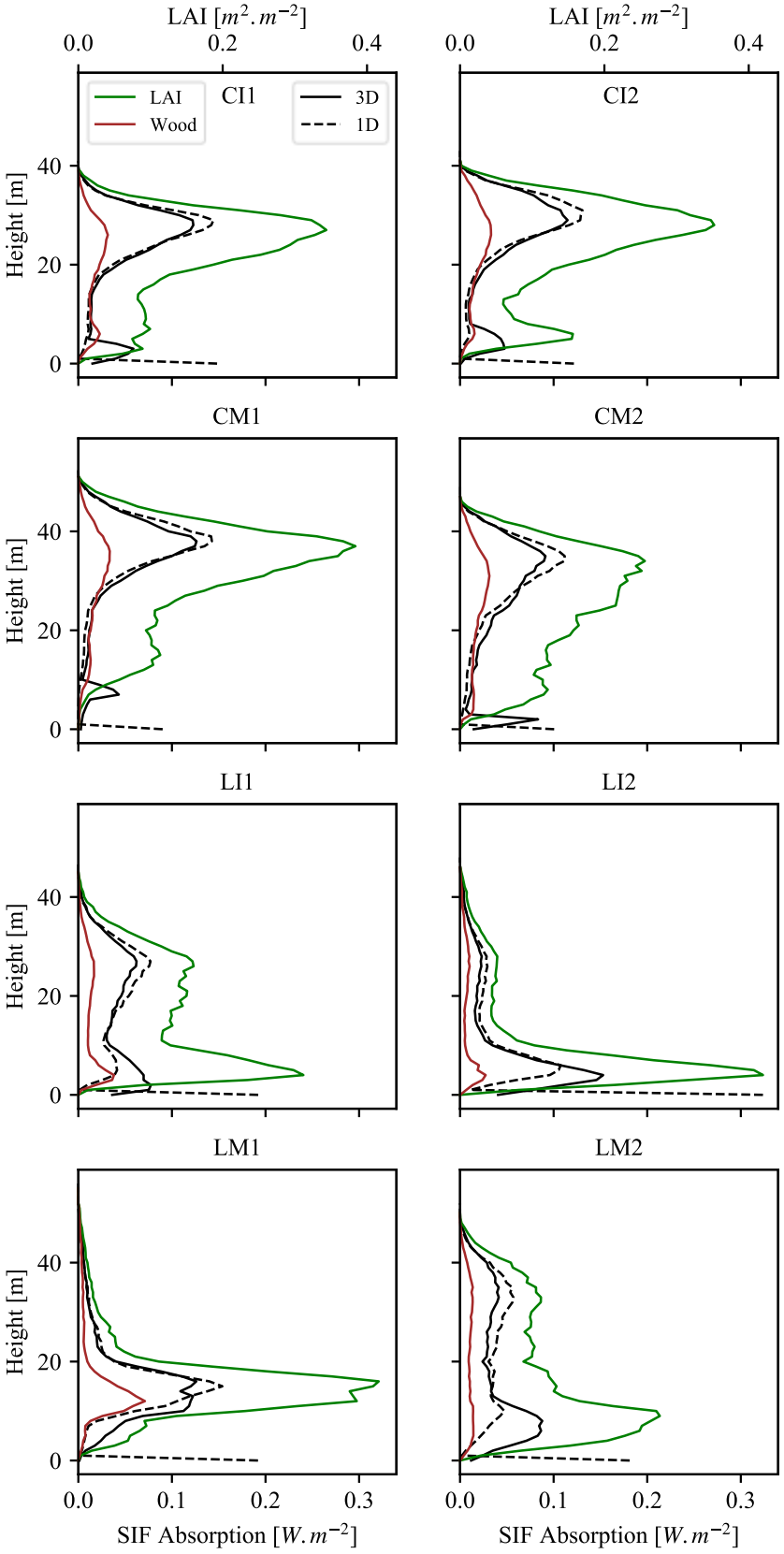

Figure 14.Vertical profiles of LAI, woody elements and SIF absorption in 3D and 1D forest abstractions, at 12.00 (local time).

3.5. Impact of forest 3D structure on SIF nadir yield (2nd and 3rd processes)

Figure 15 shows diurnal values of SIF nadir yield for 3D and 1D forest plots and their relative error $\varepsilon_{SIF.NY,1D-3D}(t)$. SIF nadir yield informs on the potential of nadir viewing remote sensing instruments to observe leaf SIF emission. The diurnal evolution of $\varepsilon_{SIF.NY,1D-3D}$ is similar to the diurnal evolution of total nadir SIF radiance relative error $MARE_{SIF,L_v,1D-3D}$ (Figure 5): larger errors occur in early morning around 8:00 and late afternoon around 18:00, with minimal errors at noon. SIF yield of 1D plots is always overestimated. Also, errors are larger at 640 nm - 700 nm than at 700 - 850 nm. This is due to the lower impact of multiple scattering at 640 - 700 nm than at 700 - 850 nm and therefore the larger impact of shadowing effects at 640 - 700 nm.

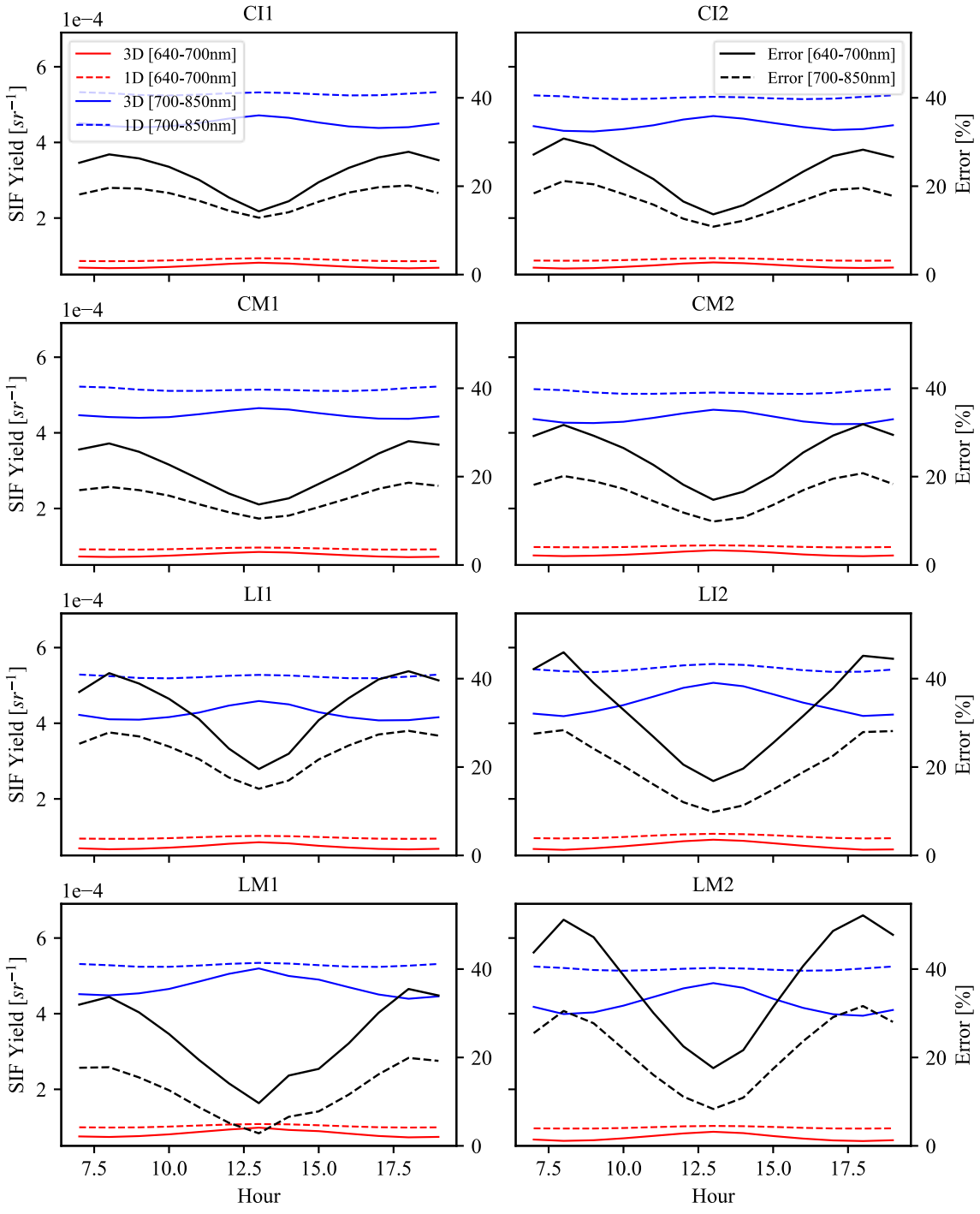

Figure 15. Diurnal SIF nadir yield of 3D and 1D plots and relative errors at 640 - 700 nm and 700 - 850 nm.

3.6. Influence of woody elements

Figure 16 illustrates the impact of woody elements (*i.e.*, branches and trunks) on the canopy SIF signal. It shows PSI, PSII and total SIF nadir spectral radiance at 12.00 of local time for CM1 and LM1 3D plots simulated with (W) and without (NW) woody elements, and also the

associated relative errors $\varepsilon_{SIF,L,NW-W}(\lambda)$ for the total SIF nadir radiance. SIF radiance is significantly higher if wood is neglected in DART simulations, especially in the near-infrared domain. $\varepsilon_{SIF,L_v,NW-W}(\lambda)$ is larger (≈25%) at wavelengths above 750nm, and smaller at wavelengths smaller than 680nm. This is explained by the fact that there is more multiple scattering at these wavelengths, which in turn increases the probability of interception of SIF radiation by woody elements.

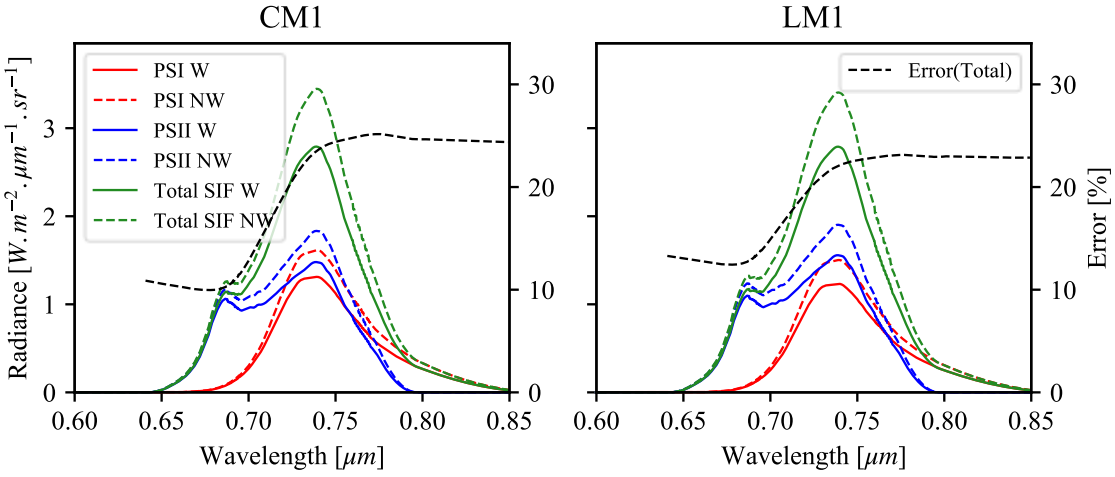

Figure 16. PSI, PSII and total SIF nadir spectral radiance and error $\varepsilon_{SIF,L_v,NW\text{-}W}(\lambda)$ of 3D CM1 and LM1 plots simulated with (W) and without (NW) woody elements at 12.00 (local time)

The diurnal relative error of the SIF total nadir radiance for CM1 and LM1 3D plots simulated without woody elements, compared to presence of woody elements, varies over the course of the day (Figure 17). It is lowest at solar noon for LM1 and relatively stable for CM1. The time variability for LM1 is explained by the fact that its leaf and wood densities are in the canopy upper layers, which increases the influence of horizontal heterogeneity, and consequently the occurrence of smaller errors at noon. Conversely, for CM1, the leaf and wood densities are larger at lower tree heights, which leads to smaller horizontal heterogeneity effects, including smaller shadow effects.

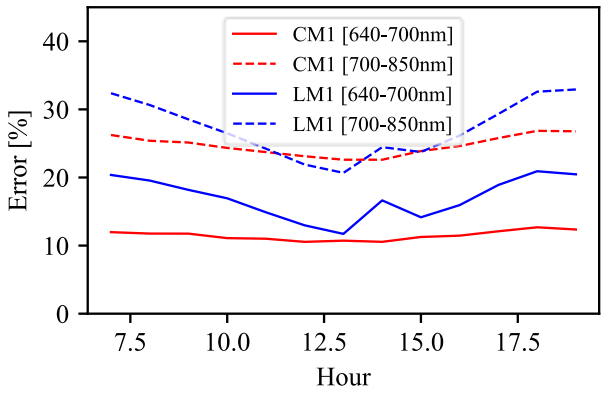

Figure 17. Diurnal relative error of total nadir SIF radiance $MARE_{SIF,L_v,NW-W}(t)$ of the CM1 and LM1 3D forest plots simulated without woody elements. 640 – 700 nm and 700 – 850 nm.

The influence of woody elements on the remotely sensed SIF signal can be split into shading and blocking effects. These effects are not independent. The shading effect corresponds to the shading of leaves by woody elements during the direct sun and atmosphere illumination of the forest scene. It limits the absorption of PAR by chlorophylls and consequently decreases leaf SIF emission (*i.e.*, 1st process). The blocking effect corresponds to the interception (*i.e.*, absorption and scattering) by woody elements of SIF radiation from its leaf emission to the exit of the forest canopy along the viewing direction of the remote sensing sensor. Figure 18 illustrates the magnitude of the shading effect. It shows the DART simulated diurnal $APAR_{green}(t)$ and the associated relative error $\varepsilon_{APAR,NW-W}(t)$, for the CM1 and LM1 3D plots with and without woody elements. $APAR_{green}$ is always larger for the plots without wood, as expected. The relative error associated to the shading effect greatly varies over the selected day. It is minimal at solar midday, when trunks and branches are blocking the least amount of direct solar radiation, and largest in early morning and late afternoon when trunks and branches are blocking a larger part of direct PAR. Figure 19 illustrates the blocking effect. It shows the diurnal SIF nadir escape factor at [400nm-700nm] and [700nm-850nm] for the CM1 and LM1 3D plots simulated with (W) and without (NW) woody elements, and the associated relative error $\varepsilon_{SIF.NEF,NW-W}(t)$. This relative error is nearly constant over the day, conversely to the relative error on the canopy $APAR_{green}$. Indeed, as a first approximation $SIF_{nadir\ EF}$ corresponds to a quantity that is relatively constant: the sum of the canopy "direct – direct" and "diffuse – direct" transmittance (Vermote et al., 1997) weighted by a normalized vertical distribution of leaf SIF emitted radiation. The "diffuse – direct" transmittance is much smaller at [640-700nm] than at [700nm-850nm] because vegetation absorbs much more at [640-700nm] than at [700nm-850nm]. Since the blocking effect of wood is more pronounced for oblique

directions, it has a higher impact on the "diffuse – direct" than on the "direct – direct" transmittance. This explains that $\varepsilon_{SIF.NEF,NW-W}(t)$ is smaller at [640-700nm] than at [700nm-850nm].

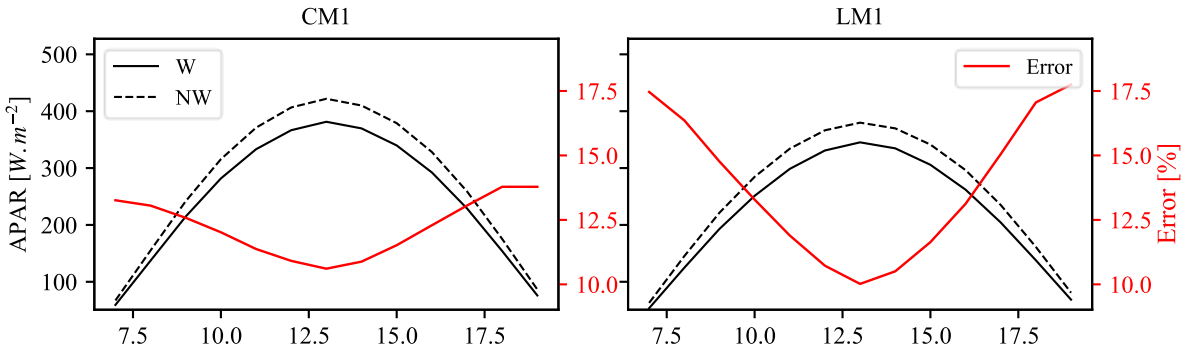

Figure 18. Diurnal $APAR_{green}$ of CM1 and LM1 3D forest plots with (Wood) and without (No Wood) woody elements and their associated relative errors $\varepsilon_{APAR,NW-W}(t)$.

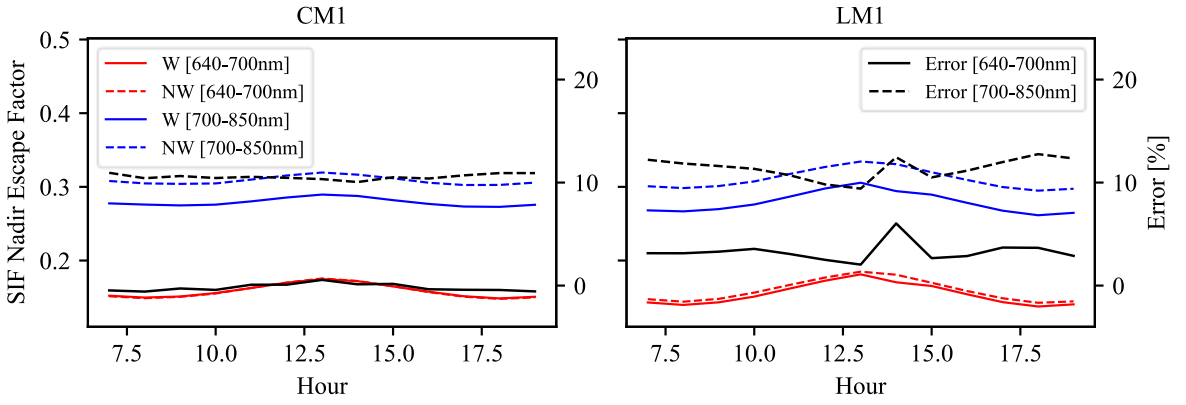

Figure 19. Diurnal SIF nadir escape factor over [640nm-700nm] and [700nm-850nm] of CM1 and LM1 3D plots simulated with (W) and without (NW) woody elements and associated relative error $\varepsilon_{SIF.NEF,NW-W}(t)$.

4. Discussion

4.1. 3D structure of the forest study sites

The comparison of DART simulated SIF and non SIF radiometric quantities of 1D and 3D abstractions of the studied forest plots highlights the influence of the forest architecture, and especially the forest horizontal heterogeneity, on these quantities: $APAR_{green}$ ($\varepsilon_{APAR,1D-3D}(t)$: Figure 8), SIF emitted ($\varepsilon_{SIF.em,1D-3D}(t)$: Figure 10), $SIF_{nadir\ yield}$ ($\varepsilon_{SIF.NY,1D-3D}(t)$: Figure 15), canopy SIF exitance and escape factor ($\varepsilon_{SIF.EF,1D-3D}(t)$: Figure 12), SIF nadir yield ($\varepsilon_{SIF.NY,1D-3D}(t)$: Figure 15) and reflectance (Figure 6). Braghiere et al. (2021) found that the

SIF modeling was improved by introducing a clumping index (Nilson, 1971; Pinty et al., 2006) to replicate the behavior of structurally complex 3D canopies in the 1D model CliMA-Land (based on the mSCOPE model (Yang et al., 2017)). In this study, simulating the SIF signal while neglecting the forest horizontal heterogeneity can lead to very large relative errors, especially for logged "L" forest sites where they can reach 60%. For example, the error on SIF radiance $MARE_{SIF,L_v,1D-3D}(t)$ is higher for the logged "L" forest sites (Figure 5). This is consistent with the fact that these forest sites have a higher horizontal heterogeneity, with a higher canopy height variability and a higher number of pure bare ground pixels, as shown in Table 4 and in the height maps (Figure 2). Generally, the horizontal heterogeneity tends to decrease the SIF signal that escapes the forest canopy. The vertical heterogeneity appeared to have an opposite effect in most cases. These points are further discussed below.

4.2. Effect of 3D architecture on the three processes driving SIF generation

Several sensitivity analysis studies based on radiative transfer modeling were carried out to assess the impact of some structural parameters on the SIF such as leaf density, leaf angular distribution and fractional vegetation cover (Tong et al., 2021; Zeng et al., 2020), the contribution of understory (Hornero et al., 2021), clumping and woody elements impacts (Malenovský et al., 2021). In this study, we assessed the impact of canopy heterogeneity on SIF and processes driving its generation. High relative errors in nadir SIF radiance were observed for the 8 forest plots due to neglecting the 3D forest architecture, in particular, the horizontal heterogeneity. Errors were maximal in the hours of the day with lowest PAR having the larger shading effects. They were higher than 50% in the most heterogeneous plots (LI2 and LM2) and at [640-700nm] where shading effects are higher due to the lower importance of multiple scattering in the canopy. The errors in the canopy SIF radiance where forest horizontal architecture was neglected (*i.e.*, 1D forest plots) can be explained by two processes that drive the SIF signal generation.

1) $APAR_{green}$ is overestimated if the forest horizontal architecture is neglected. It leads to an overestimation of the SIF emitted by leaves. This overestimation of SIF emission mainly occurs in the upper canopy layers. This is mainly due to the fact that in the forest 1D abstractions, the leaves of the top layers are homogeneously distributed, whereas in actual 3D forests, they can be greatly clumped at two levels: they are grouped within distinct tree

crowns, and also, they tend to be clumped within each tree crown. Combined, these effects result in upper layers of 1D plots that are more efficiently illuminated than in 3D plots, which explains higher SIF emission in 1D plots than in 3D plots. However, in the bottom layers, the SIF emission of 1D plots is underestimated. Indeed, the roughness of the actual canopy causes a better penetration of light to the bottom layers of the 3D plots, compared to the associated 1D plots, where the top layers of the canopy shade more efficiently the light. This is illustrated by Figure 11: the profile of SIF emission is similar to the profile of LAI with a higher $\frac{\mathrm{SIF_{emitted}}}{\mathrm{LAI}}$ value in the top layers. This means that the SIF emission per leaf area unit is higher for the top layers because leaves in the top layers are able to capture more light than the leaves in the bottom layers.

2) The emitted SIF radiation has a higher ability to escape from the canopy in the 1D abstractions of the forest plots both for the upward nadir direction (*cf.* SIF yield in Figure 15), and for the upper hemisphere (*cf.*, SIF escape factor$_{hemi}$ in Figure 12). It corresponds to an underestimation of the total absorption fraction of SIF in all 1D abstractions of the 8 forest plots (Table 6, Table 7). This underestimation of SIF absorption is rather large for the ground, and larger for [640-700nm] (*i.e.*, between -17 and -43% for [640-700nm], between -5% and -35% for [700-850nm]) and rather small for "Leaf + Wood" (i.e., between -2 and -4% for [640-700nm], between -1 and -3% for [700-850nm]). LM1 has a slightly different behavior: in its 1D abstraction, the absorption of "Leaf + Wood" is slightly overestimated for [700-850nm] (*i.e.*, around 2%). Part of the underestimation of SIF absorption by the ground for 1D plots is due to the smaller area of the ground in the 1D plot compared to the 3D plot where topography is simulated (Table 2).

The vertical profiles of SIF emission (Figure 11) and absorption (Figure 14) of the 1D plots show that emission and absorption are both overestimated in the top layers and underestimated in the bottom layers. A main particularity for the absorption profile is the influence of the ground. It shows sharp peaks at 0 m height for 1D simulations. For the 3D abstractions of the forest plots, the height of the ground is variable. Therefore, ground absorption peaks appear in the bottom for the “C” plots. These peaks are not visible in “L” plots, because of important absorption of the leaves and woody elements in the bottom part of the canopies.

4.3. Influence of 3D architecture on the canopy reflectance.

As a first approximation, SIF emission can be considered as the reflection of radiation at a different wavelength from that of the incident radiation. Therefore, it makes sense to find similar errors for SIF radiance $MARE_{SIF,L_v,1D-3D}(t)$ and canopy reflectance $MARE_{\rho,1D-3D}(t)$. However, SIF has some particularities that may differ from reflectance. Indeed, the SIF emission only comes from leaf elements. Other components of the canopy (*i.e.*, woody elements and ground) do not emit SIF radiation, even though they contribute indirectly by scattering SIF radiation emitted by foliar elements. On the other hand, all elements of the canopy can contribute directly to the canopy radiance. Since bare ground does not directly contribute to the SIF radiance of forest plots, pure bare ground pixels have SIF radiance values close to zero. A nadir viewing sensor cannot see the bare ground in 1D plots, conversely to 3D plots. Hence, $MARE_{SIF,L_v,1D-3D}$ tends to be larger than $MARE_{\rho,1D-3D}$ because for canopy reflectance, pure bare ground pixels and vegetation pixels have values of the same order of magnitude. This explains that for LI2, the SIF radiance errors (Figure 5) are notably larger than the reflectance errors (Figure 7). Indeed, compared to the other sites (cf. Table 4), the LI2 site has the particularity to have the largest surface of ground without vegetation cover. Therefore, its $MARE_{SIF,L_v,1D-3D}$ tends to be large, especially if the ground reflectance is high. Multiple scattering explains that SIF radiance errors are larger in 640 – 700nm than in 700-850nm domain. Indeed, in the 700 – 850nm, the shadowing effects due to the canopy structure are attenuated by the important multiple scattering in this spectral domain. It is also the case for canopy reflectance in most cases expect for LI1 (in the middle of the day) and LI2 (Figure 7). This is because we only consider the 640 – 700nm spectral region and not all the 400 – 700nm for the comparison with SIF. Indeed, In Figure 6, we see that for these plots, $\varepsilon_{\rho,1D-3D}(\lambda)$ has a local minimum around 680nm, and even a sign change for LI2.

4.4. Influence of woody elements

Although woody elements do not generate SIF emission, their interaction with the photosynthetically active light and with SIF radiation emitted by leaves can highly impact the SIF signal, as shown in (Malenovský et al., 2021). We studied their influence on the SIF signal by comparing the SIF signal of forest plots that was simulated without and with woody elements. For that, we removed the woody elements from the 3D abstractions of the CM1 and LM1 plots. It appeared that the plots without woody elements had a higher simulated SIF radiance,

662 especially in the 700-850 nm spectral domain where multiple scattering is highly influenced by
663 the presence of woody elements. The influence of woody elements is smaller in the 640 – 700
664 nm spectral domain. The shading effect of woody elements on SIF emission leads to a lower
665 $APAR_{green}$ (Figure 18) and therefore triggering less SIF emission. It was shown to be more
666 important than the blocking effect of woody elements (Figure 19), especially for oblique solar
667 directions and at 640-700 nm.

668

669 **5. Concluding remarks**

670 This study investigated the potential effect of the forest 3D architecture on diurnal nadir SIF
671 RS observations and SIF emissions inside the canopy. We studied the following three processes
672 responsible for modulation of the canopy SIF signal: i) the attenuation of incident PAR in the
673 canopy, ii) the leaf SIF emission efficiency, and iii) the attenuation of the SIF between its place
674 of emission and its observation above the canopy. The potential impact of woody elements on
675 the SIF signal of forest stands was also investigated. Eight study sites, located within the
676 temperate deciduous forest in the Smithsonian Environmental Research Center, were modeled
677 using the DART-FT and DART-Lux radiative transfer modes and the effects of their forest
678 architecture were assessed by comparing SIF quantities of the sites simulated as 3D, 1D and
679 0D scenes.

680 Although several general trends common to all sites were clearly identified, some results
681 were of the site-specific nature due to structural differences in canopy horizontal and vertical
682 heterogeneity. Results revealed that the horizontal heterogeneity of forests had a larger
683 influence than the canopy vertical heterogeneity. Therefore, for a correct modeling of remotely
684 sensed SIF signals of spatially heterogeneous canopies, one must consider the full 3D
685 architecture of forests and not only their vertical heterogeneity as being assumed in 1D RTMs.

686 Studying the propagation of SIF radiation within the canopy through quantitative
687 parameters, such as the SIF escape factor and the nadir SIF yield, is essential for linking the
688 SIF RS observation to the canopy foliage SIF emission. Three key indicators were able to
689 explain most of the differences between the nadir SIF signal of canopies simulated as 3D and
690 1D landscapes. The SIF escape factor (ε_{1D-3D} up to 40%) was shown to be the most indicative
691 parameter, followed by the attenuation of incident PAR and consequently reduction of
692 $fAPAR_{green}$ (ε_{1D-3D} less than 5%), and the SIF emission yield (ε_{1D-3D} less than 2%) induced
693 by different *fqe* values assigned to the sun- and shade-adapted leaves. Our results indicated that

694 the influence of forest architecture on SIF escape factor and nadir SIF yield values (ε up to 40%)
695 varies in time, with differences in forest stand structure and per spectral domain, with ε being
696 always greater for the wavelength range of 640 – 700 nm than for the range of 700 – 850 nm.
697 The presence of woody elements inside DART-simulated forest scenes appeared to have
698 a relatively large influence on the canopy SIF radiance through the two effects: i) a shading of
699 photosynthetically active foliage and ii) a blocking (obstruction) of SIF radiation. The relative
700 error associated with the neglection of wood existence ranged between 10% and 35%,
701 depending on analyzed spectral domain and forest site, where the relative errors for the shading
702 effect were ranging between 10 and 20%, and for the blocking effect between 0 and 10%.
703 Although this work underlines the usefulness of 3D RTMs for investigating physical
704 bases linking RS SIF observations with SIF emitted inside a forest canopy, there are several
705 modeling aspects that should be reconsidered and improved in the follow-up work. For example,
706 leaf SIF emission properties were assumed to be constant throughout the day, *i.e.*, the actual
707 modulation of SIF emission by local environmental conditions (*e.g.*, leaf temperature, air
708 humidity, etc.) was not considered. Remediation of this strong assumption requires inclusion of
709 a full canopy energy balance in the DART modeling scheme, that would allow to account for
710 crucial environmental parameters of radiative (*i.e.*, visible, near infrared and thermal infrared
711 radiation budgets) as well as non-radiative processes (*e.g.*, photosynthesis). This is currently
712 possible only by coupling DART with a 1D energy budget model like SCOPE. The development
713 of a 3D energy balance modeling, based on DART radiation budget computations, is on the list
714 of our future works. Three major DART-Lux modeling works, partly completed, will also be very
715 helpful for rapid simulations of SIF over larger landscapes: SIF and thermal emission of
716 vegetation simulated as turbid medium, and 3D radiative budget, including SIF emission.
717

718 **Acknowledgements**

719 This work was funded as the “Fluo3D” project by the TOSCA program of the French National
720 Space Agency (Centre National d'Etudes Spatiales), with financial support from the CNRS
721 through the 80|Prime program.). The authors are grateful to the Australian Research Council
722 Future Fellowship ‘Bridging Scales in Remote Sensing of Vegetation Stress’ (FT160100477)
723 for support of Z. Malenovský, to W. Liu from Fujian Agriculture and Forestry University for
724 providing leaf fluorescence quantum efficiencies for forests, to Geoffrey G. Parker from SERC
725 for providing the geolocations and management categories of the selected study sites and to

Petya K. Campbell from NASA Goddard Space Flight Center and University of Maryland for providing leaf biochemical properties measured for the selected SERC forest species and her contribution to the improvement of the manuscript.

Appendix 1: Conversion of turbid voxels into triangles clouds.

Each turbid cell of a forest mock-ups is converted to a linear combination of a few 3D objects (i.e., made of facets) among N cell objects whose LAI is LAI_n, with $n \in [1\ \ N]$. Accuracy on the simulated LAI is 10^{-2} with N = 16 with LAI_n equal to 0.01, 0.02, 0.05, 0.1, 0.2, 0.3, 0.4, 0.5, 1, 1.5, 2, 2.5, 3, 3.5, 4, and 4.5. The area of a facet in each cell object is 5.10^{-5} m^2 if $LAI_n \leq 2$, and 10^{-4} m^2 if $LAI_n > 2$.

The algorithm of the conversion method is based on the value of LAI_{cell} of the turbid cell to convert:

* Scene $LAI_{cell} < 1$: the turbid cell is replaced by two 3D cell objects at most:
  - 1st cell object (i.e., cell object with the larger LAI): it can be only enlarged. Its enlargement is 5% at most. If it should be 5% to get the exact LAI of the turbid cell, then a 2nd cell is introduced.
  - 2nd cell object: it can be enlarged or shrunk.
* Scene $LAI_{cell} > 1$: the turbid cell is replaced by three cell objects cells at most:
  - 1st cell object: it cannot be scaled. If precision $< 10^{-2}$, then a 2nd cell is used.
  - 2nd cell object: it can be only enlarged, by 5% at most. A 3rd cell is used if a larger enlargement is needed.
  - 3rd cell object: it can be enlarged or shrunk.

Examples of replacement of a turbid cell (LAI_{cell}) by up to 3 3D cell objects:

- $LAI_{cell} = 0.92$ (Figure 20). Replacing it by a cell object of LAI = 1, (*i.e.*, shrinking it by a factor 0.96) would create 2 cm wide empty spaces at the cell borders. Therefore, it was instead replaced by a cell object of LAI=0.5 and a cell object of LAI = 0.4 enlarged by a factor 1.025. (*i.e.*, $0.92 \approx 0.5 + 0.4 \times 1.025^2$).
- $LAI_{cell} = 0.23$ ($\approx 0.2 + 0.02 \times 1.2247^2$) $\Rightarrow$ 2 cell objects: $LAI_n = 0.2$, $LAI_n = 0.02$ scaled by 1.2247
- $LAI_{cell} = 0.48$ ($\approx 0.4 + 0.1 \times 0.8944^2$) $\Rightarrow$ 2 cell objects: $LAI_n = 0.4$, $LAI_n = 0.1$ shrunk by 0.8944

- LAI_{cell} = 0.93 ($\approx 0.5 + 0.4 \times 1.0368^2$) $\Rightarrow$ 2 cell objects: LAI_n=0.5, LAI_n=0.4 scaled by 1.0368
- LAI_{cell} = 0.64 ($\approx 0.5 + 0.1 + 0.05 \times 0.8944$) $\Rightarrow$ 3 cell objects: LAI_n = 0.5, LAI_n= 0.1, LAI_n= 0.05 shrunk by 0.8944.

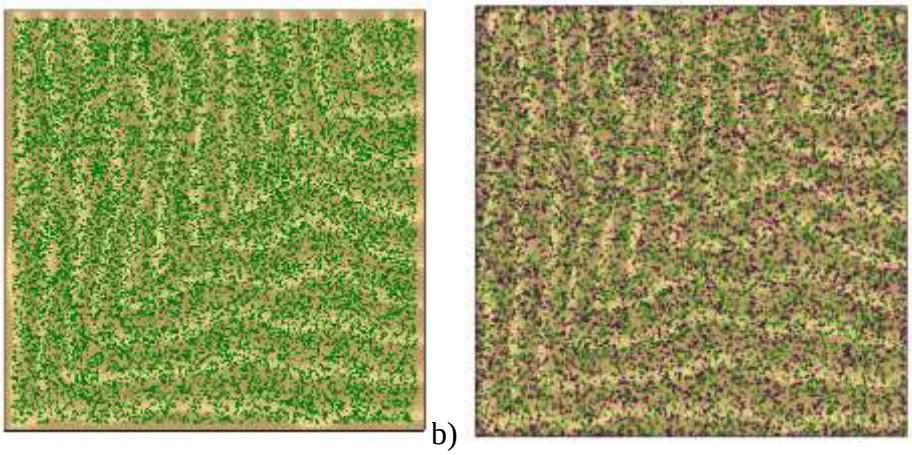

a) b)

Figure 20. Top view of a turbid cell of LAI = 0.92 simulated with N cell objects. a) N=1: cell object of LAI = 1 is shrunk by a factor 0.96, resulting in empty space along the borders of the cell. b) N=2: 3D object of LAI = 0.5 (green) + 3D object of LAI = 0.4 enlarged by a factor 1.025 (purple).

This conversion method ensures that the mock-up is represented by a finite number of 3D objects (i.e., 16x3 = 48). It also avoids the appearance of holes due to shrinking the 3D objects, and large exceeding of voxel limits due to the enlargement of 3D objects. M = 3 samples of each cell object are randomly used to introduce a random variability in the mock-ups. Also, a random rotation of 0°, 90°, 180° or 270° relative to the vertical axis ensures more randomness of the simulated cell.

Appendix 2: Equivalence between DART-FT and DART-Lux simulations

Our work combines DART-FT simulations of radiative budget and DART-Lux simulations of scene radiance / reflectance. Therefore, the consistency of these two DART modes is an essential point. Relative differences of DART-FT and DART-Lux can be as small as 10^{-5} depending on their modeling parameters of each mode. For example, the number of discrete directions for DART-FT, and the number of samples per pixel for DART-Lux. Here, this similarity is illustrated

through the comparison of the reflectance and SIF radiance of LM1, using model parameters hat were used in our work. Figure 21 indicates that MARE is equal to 1.3% for scene reflectance, 2.1% for PSI radiance, and 1.72% for PSII radiance.

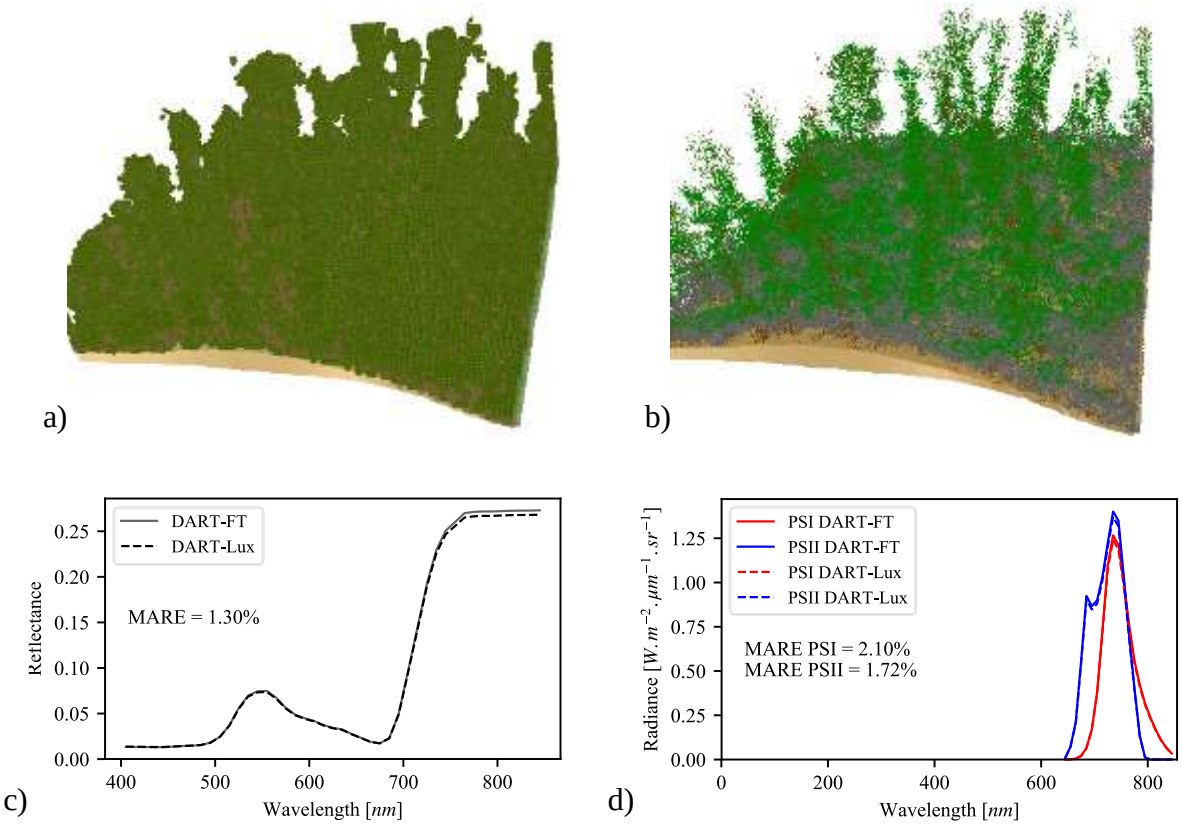

Figure 21: Comparison of DART-FT (turbid voxels) and DART-Lux (turbid voxels transformed to triangles) for a 10m x 10m subscene of CI1. a) LM1 turbid mock-up. b) LM1 triangles cloud mock-up (after conversion). Green: sun-adapted leaves, Grey: shade-adapted leaves, Brown: woody elements. c) DART-FT and DART-Lux scene reflectance. d) Scene PSI and PSII radiance simulated by DART-FT and DART-Lux.

References

Ač, A., Malenovský, Z., Olejníčková, J., Gallé, A., Rascher, U., & Mohammed, G. (2015). Meta-analysis assessing potential of steady-state chlorophyll fluorescence for remote sensing detection of plant water, temperature and nitrogen stress. *Remote Sensing of Environment*, *168*, 420–436. https://doi.org/10.1016/j.rse.2015.07.022

Baker, N. R. (2008). Chlorophyll Fluorescence: A Probe of Photosynthesis In Vivo. *Annual Review of Plant Biology*, *59*(1), 89–113. https://doi.org/10.1146/annurev.arplant.59.032607.092759

Braghiere, R. K., Wang, Y., Doughty, R., Sousa, D., Magney, T., Widlowski, J.-L., Longo, M., Bloom, A. A., Worden, J., Gentine, P., & Frankenberg, C. (2021). Accounting for canopy structure improves hyperspectral radiative transfer and sun-induced chlorophyll fluorescence representations in a new generation Earth System model. *Remote Sensing of Environment*, *261*, 112497. https://doi.org/10.1016/j.rse.2021.112497

Brede, B., Verrelst, J., Gastellu-Etchegorry, J.-P., Clevers, J. G. P. W., Goudzwaard, L., den Ouden, J., Verbesselt, J., & Herold, M. (2020). Assessment of Workflow Feature Selection on Forest LAI Prediction with Sentinel-2A MSI, Landsat 7 ETM+ and Landsat 8 OLI. *Remote Sensing*, *12*(6), Article 6. https://doi.org/10.3390/rs12060915

Campbell, P. K. E., Huemmrich, K. F., Middleton, E. M., Ward, L. A., Julitta, T., Daughtry, C. S. T., Burkart, A., Russ, A. L., & Kustas, W. P. (2019). Diurnal and Seasonal Variations in Chlorophyll Fluorescence Associated with Photosynthesis at Leaf and Canopy Scales. *Remote Sensing*, *11*(5), Article 5. https://doi.org/10.3390/rs11050488

Campbell, P. K. E., Middleton, E. M., McMurtrey, J. E., Corp, L. A., & Chappelle, E. W. (2007). Assessment of vegetation stress using reflectance or fluorescence measurements. *Journal of Environmental Quality*, *36*(3), 832–845. https://doi.org/10.2134/jeq2005.0396

Campbell, P. K. E., Ward, L. A., Huemmrich, K. F., & Middleton, E. (2018). Diurnal and seasonal dynamics in chlorophyll fluorescence, xanthophyll cycle and photosynthetic function, at leaf and canopy scales. *AGU Fall Meeting Abstracts*, *33*. http://adsabs.harvard.edu/abs/2018AGUFM.B33C..07C

819 Cook, B. D., Corp, L. A., Nelson, R. F., Middleton, E. M., Morton, D. C., McCorkel, J. T.,
820 Masek, J. G., Ranson, K. J., Ly, V., & Montesano, P. M. (2013). NASA Goddard's
821 LiDAR, Hyperspectral and Thermal (G-LiHT) Airborne Imager. *Remote Sensing*,
822 *5*(8), Article 8. https://doi.org/10.3390/rs5084045

823 Damm, A., Guanter, L., Paul-Limages, E., Tol, C. van der, Hueni, A., Buchmann, N., Eugster,
824 W., Ammann, C., & Schaepman, M. E. (2015). Far-red sun-induced chlorophyll
825 fluorescence shows ecosystem - specific relationships to gross primary production: An
826 assessment based on observational and modeling approaches. *Remote Sensing of*
827 *Environment*, *166*, 91–105. https://doi.org/10.1016/j.rse.2015.06.004

828 Drusch, M., Moreno, J., Bello, U. D., Franco, R., Goulas, Y., Huth, A., Kraft, S., Middleton,
829 E. M., Miglietta, F., Mohammed, G., Nedbal, L., Rascher, U., Schüttemeyer, D., &
830 Verhoef, W. (2017). The FLuorescence EXplorer Mission Concept—ESA's Earth
831 Explorer 8. *IEEE Transactions on Geoscience and Remote Sensing*, *55*(3), 1273–1284.
832 https://doi.org/10.1109/TGRS.2016.2621820

833 Fournier, A., Daumard, F., Champagne, S., Ounis, A., Goulas, Y., & Moya, I. (2012). Effect
834 of canopy structure on sun-induced chlorophyll fluorescence. *ISPRS Journal of*
835 *Photogrammetry and Remote Sensing*, *68*, 112–120.
836 https://doi.org/10.1016/j.isprsjprs.2012.01.003

837 Gastellu-Etchegorry, J.-P., Demarez, V., Pinel, V., & Zagolski, F. (1996). Modeling radiative
838 transfer in heterogeneous 3-D vegetation canopies. *Remote Sensing of Environment*,
839 *58*(2), 131–156. https://doi.org/10.1016/0034-4257(95)00253-7

840 Gastellu-Etchegorry, J.-P., Lauret, N., Yin, T., Landier, L., Kallel, A., Malenovský, Z., Bitar,
841 A. A., Aval, J., Benhmida, S., Qi, J., Medjdoub, G., Guilleux, J., Chavanon, E., Cook,
842 B., Morton, D., Chrysoulakis, N., & Mitraka, Z. (2017). DART: Recent Advances in
843 Remote Sensing Data Modeling With Atmosphere, Polarization, and Chlorophyll
844 Fluorescence. *IEEE Journal of Selected Topics in Applied Earth Observations and*
845 *Remote Sensing*, *10*(6), 2640–2649. https://doi.org/10.1109/JSTARS.2017.2685528

846 Gastellu-Etchegorry, J.-P., Yin, T., Lauret, N., Cajgfinger, T., Gregoire, T., Grau, E., Feret, J.-
847 B., Lopes, M., Guilleux, J., Dedieu, G., Malenovský, Z., Cook, B. D., Morton, D.,
848 Rubio, J., Durrieu, S., Cazanave, G., Martin, E., & Ristorcelli, T. (2015). Discrete
849 Anisotropic Radiative Transfer (DART 5) for Modeling Airborne and Satellite

Spectroradiometer and LIDAR Acquisitions of Natural and Urban Landscapes. *Remote Sensing*, *7*(2), Article 2. https://doi.org/10.3390/rs70201667

Gastellu-Etchegorry, J.-P., Yin, T., Lauret, N., Grau, E., Rubio, J., Cook, B. D., Morton, D. C., & Sun, G. (2016). Simulation of satellite, airborne and terrestrial LiDAR with DART (I): Waveform simulation with quasi-Monte Carlo ray tracing. *Remote Sensing of Environment*, *184*, 418–435. https://doi.org/10.1016/j.rse.2016.07.010

Georgiev, I., Křivánek, J., Davidovič, T., & Slusallek, P. (2012). Light transport simulation with vertex connection and merging. *ACM Transactions on Graphics*, *31*(6), 192:1-192:10. https://doi.org/10.1145/2366145.2366211

Givnish, T. J. (1988). Adaptation to Sun and Shade: A Whole-Plant Perspective. *Functional Plant Biology*, *15*(2), 63–92. https://doi.org/10.1071/pp9880063

Guanter, L., Zhang, Y., Jung, M., Joiner, J., Voigt, M., Berry, J. A., Frankenberg, C., Huete, A. R., Zarco-Tejada, P., Lee, J.-E., Moran, M. S., Ponce-Campos, G., Beer, C., Camps-Valls, G., Buchmann, N., Gianelle, D., Klumpp, K., Cescatti, A., Baker, J. M., & Griffis, T. J. (2014). Global and time-resolved monitoring of crop photosynthesis with chlorophyll fluorescence. *Proceedings of the National Academy of Sciences*, *111*(14), E1327–E1333. https://doi.org/10.1073/pnas.1320008111

Hernández-Clemente, R., North, P. R. J., Hornero, A., & Zarco-Tejada, P. J. (2017). Assessing the effects of forest health on sun-induced chlorophyll fluorescence using the FluorFLIGHT 3-D radiative transfer model to account for forest structure. *Remote Sensing of Environment*, *193*, 165–179. https://doi.org/10.1016/j.rse.2017.02.012

Hornero, A., North, P. R. J., Zarco-Tejada, P. J., Rascher, U., Martín, M. P., Migliavacca, M., & Hernandez-Clemente, R. (2021). Assessing the contribution of understory sun-induced chlorophyll fluorescence through 3-D radiative transfer modelling and field data. *Remote Sensing of Environment*, *253*, 112195. https://doi.org/10.1016/j.rse.2020.112195

Kallel, A. (2020). FluLCVRT: Reflectance and fluorescence of leaf and canopy modeling based on Monte Carlo vector radiative transfer simulation. *Journal of Quantitative Spectroscopy and Radiative Transfer*, *253*, 107183. https://doi.org/10.1016/j.jqsrt.2020.107183

880 Kamoske, A. G., Dahlin, K. M., Stark, S. C., & Serbin, S. P. (2019). Leaf area density from
881 airborne LiDAR: Comparing sensors and resolutions in a temperate broadleaf forest
882 ecosystem. *Forest Ecology and Management*, *433*, 364–375.
883 https://doi.org/10.1016/j.foreco.2018.11.017

884 Kobayashi, H., & Iwabuchi, H. (2008). A coupled 1-D atmosphere and 3-D canopy radiative
885 transfer model for canopy reflectance, light environment, and photosynthesis
886 simulation in a heterogeneous landscape. *Remote Sensing of Environment*, *112*(1),
887 173–185. https://doi.org/10.1016/j.rse.2007.04.010

888 Liu, W., Atherton, J., Mõttus, M., Gastellu-Etchegorry, J.-P., Malenovský, Z., Raumonen, P.,
889 Åkerblom, M., Mäkipää, R., & Porcar-Castell, A. (2019). Simulating solar-induced
890 chlorophyll fluorescence in a boreal forest stand reconstructed from terrestrial laser
891 scanning measurements. *Remote Sensing of Environment*, *232*, 111274.
892 https://doi.org/10.1016/j.rse.2019.111274

893 Liu, W., Luo, S., Lu, X., Atherton, J., & Gastellu-Etchegorry, J.-P. (2020). Simulation-Based
894 Evaluation of the Estimation Methods of Far-Red Solar-Induced Chlorophyll
895 Fluorescence Escape Probability in Discontinuous Forest Canopies. *Remote Sensing*,
896 *12*(23), Article 23. https://doi.org/10.3390/rs12233962

897 Liu, X., Guanter, L., Liu, L., Damm, A., Malenovský, Z., Rascher, U., Peng, D., Du, S., &
898 Gastellu-Etchegorry, J.-P. (2019). Downscaling of solar-induced chlorophyll
899 fluorescence from canopy level to photosystem level using a random forest model.
900 *Remote Sensing of Environment*, *231*, 110772.
901 https://doi.org/10.1016/j.rse.2018.05.035

902 Liu, Z., Lu, X., An, S., Heskel, M., Yang, H., & Tang, J. (2019). Advantage of multi-band
903 solar-induced chlorophyll fluorescence to derive canopy photosynthesis in a temperate
904 forest. *Agricultural and Forest Meteorology*, *279*, 107691.
905 https://doi.org/10.1016/j.agrformet.2019.107691

906 *LuxCoreRender – Open Source Physically Based Renderer*. (n.d.). Retrieved March 29, 2021,
907 from https://luxcorerender.org/

908 Malenovský, Z., Martin, E., Homolová, L., Gastellu-Etchegorry, J. P., Zurita-Milla, R.,
909 Schaepman, M. E., Polorný, R., Clevers, J. G. P. W., & Cudlín, P. (2008). Influence of

woody elements of a Norway spruce canopy on nadir reflectance simulated by the DART model at very high spatial resolution. *Remote Sensing of Environment*, *112*(1), 1–18. https://doi.org/10.1016/j.rse.2006.02.028

Malenovský, Z., Regaieg, O., Yin, T., Lauret, N., Guilleux, J., Chavanon, E., Duran, N., Janoutová, R., Delavois, A., Meynier, J., Medjdoub, G., Yang, P., Van der Tol, C., Morton, D., Cook, B., & Gastellu-Etchegorry, J. P. (2021). Discrete Anisotropic Radiative Transfer Modelling of Solar-induced Chlorophyll Fluorescence: Structural Impacts in Geometrically Explicit Vegetation Canopies. *Remote Sensing of Environment*.

Meroni, M., Rossini, M., Guanter, L., Alonso, L., Rascher, U., Colombo, R., & Moreno, J. (2009). Remote sensing of solar-induced chlorophyll fluorescence: Review of methods and applications. *Remote Sensing of Environment*, *113*(10), 2037–2051. https://doi.org/10.1016/j.rse.2009.05.003

Migliavacca, M., Perez-Priego, O., Rossini, M., El-Madany, T. S., Moreno, G., Tol, C. van der, Rascher, U., Berninger, A., Bessenbacher, V., Burkart, A., Carrara, A., Fava, F., Guan, J.-H., Hammer, T. W., Henkel, K., Juarez-Alcalde, E., Julitta, T., Kolle, O., Martín, M. P., … Reichstein, M. (2017). Plant functional traits and canopy structure control the relationship between photosynthetic CO2 uptake and far-red sun-induced fluorescence in a Mediterranean grassland under different nutrient availability. *New Phytologist*, *214*(3), 1078–1091. https://doi.org/10.1111/nph.14437

Mohammed, G. H., Colombo, R., Middleton, E. M., Rascher, U., van der Tol, C., Nedbal, L., Goulas, Y., Pérez-Priego, O., Damm, A., Meroni, M., Joiner, J., Cogliati, S., Verhoef, W., Malenovský, Z., Gastellu-Etchegorry, J.-P., Miller, J. R., Guanter, L., Moreno, J., Moya, I., … Zarco-Tejada, P. J. (2019). Remote sensing of solar-induced chlorophyll fluorescence (SIF) in vegetation: 50 years of progress. *Remote Sensing of Environment*, *231*, 111177. https://doi.org/10.1016/j.rse.2019.04.030

Nilson, T. (1971). A theoretical analysis of the frequency of gaps in plant stands. *Agricultural Meteorology*, *8*, 25–38. https://doi.org/10.1016/0002-1571(71)90092-6

Nobel, P. S. (1976). Photosynthetic Rates of Sun versus Shade Leaves of Hyptis emoryi Torr. *Plant Physiology*, *58*(2), 218–223. https://doi.org/10.1104/pp.58.2.218

940 North, P. R. J. (1996). Three-dimensional forest light interaction model using a Monte Carlo
941 method. *IEEE Transactions on Geoscience and Remote Sensing*, *34*(4), 946–956.
942 https://doi.org/10.1109/36.508411

943 Parker, G. G. (1995). Structure and microclimate of forest canopies. *Forest Canopies.*, 73–
944 106.

945 Pinty, B., Lavergne, T., Dickinson, R. E., Widlowski, J.-L., Gobron, N., & Verstraete, M. M.
946 (2006). Simplifying the interaction of land surfaces with radiation for relating remote
947 sensing products to climate models. *Journal of Geophysical Research: Atmospheres*,
948 *111*(D2). https://doi.org/10.1029/2005JD005952

949 Regaieg, O., Wang, Y., Malenovský, Z., Yin, T., Kallel, A., Duran, N., Delavois, A., Qi, J.,
950 Chavanon, E., Lauret, N., Guilleux, J., Cook, B., Morton, D., & Gastellu-Etchegorry,
951 J. P. (2020). Simulation of Solar-Induced Chlorophyll Fluorescence from 3D Canopies
952 with the Dart Model. *IGARSS 2020 - 2020 IEEE International Geoscience and*
953 *Remote Sensing Symposium*, 4846–4849.
954 https://doi.org/10.1109/IGARSS39084.2020.9323616

955 Rossini, M., Nedbal, L., Guanter, L., Ač, A., Alonso, L., Burkart, A., Cogliati, S., Colombo,
956 R., Damm, A., Drusch, M., Hanus, J., Janoutova, R., Julitta, T., Kokkalis, P., Moreno,
957 J., Novotny, J., Panigada, C., Pinto, F., Schickling, A., … Rascher, U. (2015). Red and
958 far red Sun-induced chlorophyll fluorescence as a measure of plant photosynthesis.
959 *Geophysical Research Letters*, *42*(6), 1632–1639.
960 https://doi.org/10.1002/2014GL062943

961 Sakai, Y., Kobayashi, H., & Kato, T. (2020). FLiES-SIF version 1.0: Three-dimensional
962 radiative transfer model for estimating solar induced fluorescence. *Geoscientific*
963 *Model Development*, *13*(9), 4041–4066. https://doi.org/10.5194/gmd-13-4041-2020

964 Tong, C., Bao, Y., Zhao, F., Fan, C., Li, Z., & Huang, Q. (2021). Evaluation of the FluorWPS
965 Model and Study of the Parameter Sensitivity for Simulating Solar-Induced
966 Chlorophyll Fluorescence. *Remote Sensing*, *13*(6), Article 6.
967 https://doi.org/10.3390/rs13061091

968 van der Tol, C., Verhoef, W., Timmermans, J., Verhoef, A., & Su, Z. (2009). An integrated
969 model of soil-canopy spectral radiances, photosynthesis, fluorescence, temperature

and energy balance. *Biogeosciences*, *6*(12), 3109–3129. https://doi.org/10.5194/bg-6-3109-2009

van der Tol, C., Vilfan, N., Dauwe, D., Cendrero-Mateo, M. P., & Yang, P. (2019). The scattering and re-absorption of red and near-infrared chlorophyll fluorescence in the models Fluspect and SCOPE. *Remote Sensing of Environment*, *232*, 111292. https://doi.org/10.1016/j.rse.2019.111292

Verhoef, W. (1984). Light scattering by leaf layers with application to canopy reflectance modeling: The SAIL model. *Remote Sensing of Environment*, *16*(2), 125–141. https://doi.org/10.1016/0034-4257(84)90057-9

Vermote, E., Tanré, D., Deuze, J., Herman, M., & Morcette, J.-J. (1997). Second Simulation of the Satellite Signal in the Solar Spectrum, 6S: An overview. *IEEE Trans. Geosci. Remote. Sens.* https://doi.org/10.1109/36.581987

Verrelst, J., Malenovsky, Z., Tol, C. van der, Camps-Valls, G., Gastellu-Etchegorry, J.-P., Lewis, P., North, P., & Moreno, J. (2019). Quantifying Vegetation Biophysical Variables from Imaging Spectroscopy Data: A Review on Retrieval Methods. *Surveys in Geophysics*, *40*(3), 589–629. https://doi.org/10.1007/s10712-018-9478-y

Verrelst, J., Rivera, J. P., van der Tol, C., Magnani, F., Mohammed, G., & Moreno, J. (2015). Global sensitivity analysis of the SCOPE model: What drives simulated canopy-leaving sun-induced fluorescence? *Remote Sensing of Environment*, *166*, 8–21. https://doi.org/10.1016/j.rse.2015.06.002

Verrelst, J., van der Tol, C., Magnani, F., Sabater, N., Rivera, J. P., Mohammed, G., & Moreno, J. (2016). Evaluating the predictive power of sun-induced chlorophyll fluorescence to estimate net photosynthesis of vegetation canopies: A SCOPE modeling study. *Remote Sensing of Environment*, *176*, 139–151. https://doi.org/10.1016/j.rse.2016.01.018

Vilfan, N., van der Tol, C., Muller, O., Rascher, U., & Verhoef, W. (2016). Fluspect-B: A model for leaf fluorescence, reflectance and transmittance spectra. *Remote Sensing of Environment*, *186*, 596–615. https://doi.org/10.1016/j.rse.2016.09.017

Vilfan, N., Van der Tol, C., Yang, P., Wyber, R., Malenovský, Z., Robinson, S. A., & Verhoef, W. (2018). Extending Fluspect to simulate xanthophyll driven leaf

reflectance dynamics. *Remote Sensing of Environment*, *211*, 345–356. https://doi.org/10.1016/j.rse.2018.04.012

Wang, Y., & Gastellu-Etchegorry, J.-P. (2021). Accurate and fast simulation of remote sensing images at top of atmosphere with DART-Lux. *Remote Sensing of Environment*, *256*, 112311. https://doi.org/10.1016/j.rse.2021.112311

Wellburn, A. R. (1994). The Spectral Determination of Chlorophylls a and b, as well as Total Carotenoids, Using Various Solvents with Spectrophotometers of Different Resolution. *Journal of Plant Physiology*, *144*(3), 307–313. https://doi.org/10.1016/S0176-1617(11)81192-2

Yang, P., van der Tol, C., Campbell, P. K. E., & Middleton, E. M. (2021). Unraveling the physical and physiological basis for the solar- induced chlorophyll fluorescence and photosynthesis relationship using continuous leaf and canopy measurements of a corn crop. *Biogeosciences*, *18*(2), 441–465. https://doi.org/10.5194/bg-18-441-2021

Yang, P., Verhoef, W., & van der Tol, C. (2017). The mSCOPE model: A simple adaptation to the SCOPE model to describe reflectance, fluorescence and photosynthesis of vertically heterogeneous canopies. *Remote Sensing of Environment*, *201*, 1–11. https://doi.org/10.1016/j.rse.2017.08.029

Yin, T., Gastellu-Etchegorry, J.-P., Lauret, N., Grau, E., & Rubio, J. (2013). A new approach of direction discretization and oversampling for 3D anisotropic radiative transfer modeling. *Remote Sensing of Environment*, *135*, 213–223. https://doi.org/10.1016/j.rse.2013.03.030

Yin, T., Lauret, N., & Gastellu-Etchegorry, J.-P. (2015). Simulating images of passive sensors with finite field of view by coupling 3-D radiative transfer model and sensor perspective projection. *Remote Sensing of Environment*, *162*, 169–185. https://doi.org/10.1016/j.rse.2015.02.020

Yin, T., Lauret, N., & Gastellu-Etchegorry, J.-P. (2016). Simulation of satellite, airborne and terrestrial LiDAR with DART (II): ALS and TLS multi-pulse acquisitions, photon counting, and solar noise. *Remote Sensing of Environment*, *184*, 454–468. https://doi.org/10.1016/j.rse.2016.07.009

Zeng, Y., Badgley, G., Chen, M., Li, J., Anderegg, L. D. L., Kornfeld, A., Liu, Q., Xu, B., Yang, B., Yan, K., & Berry, J. A. (2020). A radiative transfer model for solar induced fluorescence using spectral invariants theory. *Remote Sensing of Environment*, *240*, 111678. https://doi.org/10.1016/j.rse.2020.111678

Zhang, Z., Zhang, Y., Porcar-Castell, A., Joiner, J., Guanter, L., Yang, X., Migliavacca, M., Ju, W., Sun, Z., Chen, S., Martini, D., Zhang, Q., Li, Z., Cleverly, J., Wang, H., & Goulas, Y. (2020). Reduction of structural impacts and distinction of photosynthetic pathways in a global estimation of GPP from space-borne solar-induced chlorophyll fluorescence. *Remote Sensing of Environment*, *240*, 111722. https://doi.org/10.1016/j.rse.2020.111722

Zhang, Z., Zhang, Y., Zhang, Q., Chen, J. M., Porcar-Castell, A., Guanter, L., Wu, Y., Zhang, X., Wang, H., Ding, D., & Li, Z. (2020). Assessing bi-directional effects on the diurnal cycle of measured solar-induced chlorophyll fluorescence in crop canopies. *Agricultural and Forest Meteorology*, *295*, 108147. https://doi.org/10.1016/j.agrformet.2020.108147

Zhao, F., Dai, X., Verhoef, W., Guo, Y., van der Tol, C., Li, Y., & Huang, Y. (2016). FluorWPS: A Monte Carlo ray-tracing model to compute sun-induced chlorophyll fluorescence of three-dimensional canopy. *Remote Sensing of Environment*, *187*, 385–399. https://doi.org/10.1016/j.rse.2016.10.036

Zhao, F., Li, Y., Dai, X., Verhoef, W., Guo, Y., Shang, H., Gu, X., Huang, Y., Yu, T., & Huang, J. (2015). Simulated impact of sensor field of view and distance on field measurements of bidirectional reflectance factors for row crops. *Remote Sensing of Environment*, *156*, 129–142. https://doi.org/10.1016/j.rse.2014.09.011